



NASA Contractor Report 159160

NASA-CR-159160-VOL-1

1980 0004798

Active Flutter Control for Flexible Vehicles

Volume I Final Report

J.K. Mahesh
C.R. Stone

W.L. Garrard
P.D. Hausman

HONEYWELL INC.
Minneapolis, Minnesota 55413

CONTRACT NAS1-15486
November 1979



National Aeronautics and
Space Administration

Langley Research Center
Hampton, Virginia 23665
AC 804 827-3966

1. Report No. NASA CR-159160		2. Government Accession No.		3. Recipient's Catalog No.	
4. Title and Subtitle ACTIVE FLUTTER CONTROL FOR FLEXIBLE VEHICLES, Volume I, Final Report				5. Report Date August 1979	
				6. Performing Organization Code 41550	
7. Author(s) J. K. Mahesh W. L. Garrard C. R. Stone P. D. Hausman				8. Performing Organization Report No. F0642-FR, Vol. I	
9. Performing Organization Name and Address Honeywell Inc., Systems & Research Center 2600 Ridgway Parkway N.E., Minneapolis, MN 55413				10. Work Unit No.	
				11. Contract or Grant No. NAS1-15486	
12. Sponsoring Agency Name and Address NASA Langley Research Center Hampton, Virginia 23665				13. Type of Report and Period Covered Contractor Report	
				14. Sponsoring Agency Code	
15. Supplementary Notes NASA Technical Monitor, Mr. Henry J. Dunn					
16. Abstract An active flutter control methodology based on Linear Quadratic Gaussian theory and its application to the control of a super-critical wing is presented. Results of control surface and sensor position optimization are also discussed. Both frequency response matching and residualization are used to obtain practical flutter controllers.					
17. Key Words (Suggested by Author(s)) Active Control Methodology DAST ARW1 Wing Optimal Sensor Placement Clutter Suppression Control			18. Distribution Statement Unclassified - Unlimited N80-13053 #		
19. Security Classif. (of this report) Unclassified		20. Security Classif. (of this page) Unclassified		21. No. of Pages 79	
				22. Price*	

* For sale by the National Technical Information Service, Springfield, Virginia 22151

FOREWORD

The research described in this report was prepared by Honeywell Inc., Minneapolis, Minnesota 55413, under NASA Langley Research Center Contract NAS1-15486. This work was directed by the Flight Mechanics and Control Division of the NASA Langley Research Center and was administered by Mr. Henry J. Dunn of the Flight Mechanics and Control Division. Special thanks to Mr. Jarrel Elliot and Mr. Irving Abel for their continued support toward this contract.

The technical work reported in this volume was conducted by the Research Department at the Systems and Research Center of Honeywell Inc. Dr. A. F. Konar was the Honeywell Program Manager. Mr. C. R. Stone and Dr. J. K. Mahesh were the principal investigators on this contract. They were assisted by Mr. P. D. Hausman and Dr. W. L. Garrard. This report covers the work done from August 1978 to August 1979.

The work under this contract was reported in three volumes entitled "Active Flutter Control for Flexible Vehicles."

Volume I Final Report

Volume II Appendices

Volume III KONPACT II Program Documentation

CONTENTS

	Page
FOREWORD	iii
SECTION I INTRODUCTION	1
SECTION II ACTIVE FLUTTER CONTROL SYNTHESIS	3
METHODOLOGY	
The Flutter Design Model	3
Optimal State Feedback Design	5
Robust Kalman Estimator Design	5
Practicalization and Performance Analysis	5
KONPACT II Software for Active Control Design	6
SECTION III DYNAMIC MODELING FOR FLUTTER CONTROL	8
DESIGN	
Modeling the Dynamics of the Wing and the Aileron	9
The Actuator Dynamics	13
The Gust Model	13
The Design Model	17
SECTION IV OPTIMAL STATE FEEDBACK DESIGN AND	19
CONTROL SURFACE OPTIMIZATION	
State-Feedback Design	20
Control Surface Optimization	25
Insensitive Design	27
Control-Observe-Ability	29
SECTION V ROBUST KALMAN ESTIMATOR DESIGN AND	33
SENSOR OPTIMIZATION	
Robust Kalman Estimator Design	33
Sensor Optimization	41
SECTION VI PRACTICAL FLUTTER CONTROLLERS	50
Practicalization (Simplification) Procedure	50
Practicalization Results	53
Performance Analysis of the Final Flutter	58
Controller	

CONTENTS (CONTINUED)

	Page
SECTION VII CONCLUSIONS AND RECOMMENDATIONS.	67
Significant Results.	67
Recommendations for Future Work	68
Conclusions	69
REFERENCES	70

FIGURES

Figure		Page
1	Overall flutter system block diagram	4
2	Program organization of KONPACT II	7
3	Model geometry of the DAST ARW1 wing	8
4	State space realization of the flutter model	11
5	Root locus at $M = 0.9$ (open loop)	12
6	Implementation of actuator dynamics	14
7	Control system frequency response attenuation boundary . . .	14
8	Comparison of two dryden wind models	16
9	Block diagram of the design model.	18
10	Sirisena and baseline loci	24
11	Nyquist plot for nodes 16, 57.	37
12	Nyquist plot for node 18	39
13	Nyquist plot for node 28	40
14	DAST ARW1 node points	44
15	Bode plots for single sensor 4(2T)	56
16	Bode plots for two sensors 2 and 6.	59
17	Root locus at $M = 0.9$ (open loop).	65
18	Root locus at $M = 0.9$ (flutter suppression control)	66

TABLES

Table		Page
1	State Synthesis Summary	23
2	Control Surface Position Optimization	26
3	Best Two Accelerometers for Two Modes	32
4	Robustness Summary	36
5	Two Most Positive Zeroes	42
6	Single Sensor Robust Controller Performance	43
7	Two Sensor Robust Controller Performance	46
8	Sensor Frequency Response Matching	49
9	Single Sensor Practical Controller Performance	55
10	Two Sensor Practical Controller Performance	57
11	Practical Controller Transfer Functions	60
12	Performance Variation with Different Approximations to the DAST Half Wing (Mach No. = 0.9 \bar{q} = 7.66 k Pa) . . .	62
13	Performance Variation with Mach Number and Dynamic Pressure for the DAST Half Wing	63
14	Flutter Dynamic Pressure and Flutter Frequency Variation . . with Mach Number for the DAST Half Wing	64

SECTION I

INTRODUCTION

The general objective of this study is to develop methodology for rapid design of active control systems for flexible vehicles. Active control can help meet the goals of weight reduction and improved efficiency demanded of future flight vehicles. The methodology for active control synthesis is based on linear quadratic gaussian (LQG) theory. This is a viable method for design of multi-input multi-output controllers to meet multiple, often conflicting, performance requirements. This methodology also gives the active control designer the capability to influence the geometry of the vehicle to realize the benefits of control configured vehicle (CCV) design.

The scope of this study is to develop an active flutter control methodology, including surface/sensor placement, that will apply to a wide class of flexible vehicles and demonstrate it by designing a flutter controller for DAST ARW1 wing to increase the flutter speed by 20 percent. This study also included the development of algorithms and computer programs for flutter modeling and active control design procedures. These have been integrated into NASA owned KONPACT software (ref. 1). The resulting software is called "KONPACT II-Computer Programs for Active Control Technology."

The work under this contract was reported in three volumes entitled "Active Flutter Control for Flexible Vehicles."

Volume I. Final Report

Volume II. Appendices

Volume III. KONPACT II Program Documentation

Volume I reports the active flutter control methodology and the summary of the technical results obtained under this contract.

An overview of the Honeywell's approach to the synthesis of active flutter control for flexible vehicles is given in Section II. A brief description of KONPACT II software is also described in this section.

In Section III, the dynamic modeling of the DAST ARW1 wing for optimal flutter control design is presented. This is an automated modeling procedure which minimizes human error due to data handling.

The results of optimal state feedback synthesis for the DAST ARW1 wing are presented in Section IV. The control surface optimization results are also discussed in this section.

Section V presents the robust Kalman estimator design procedure and its application to the flutter control of the DAST ARW1 wing. Here the robustness is characterized as gain and phase margins of the overall system. Also, the sensor optimization/selection methods and results are discussed in this section.

Practicalization, of the optimal flutter controller with robust Kalman estimator, is presented in Section VI. The evaluation of the final flutter controller at different mach numbers and dynamic pressures is also presented.

Section VII contains the conclusions and recommendations.

The detailed technical results during the course of this study were documented as Customer Engineering Letters. These are collected in the form of appendices and presented in Volume II.

Volume III contains the description of the computer programs developed during this study. The user's information is also provided in that volume.

SECTION II

ACTIVE FLUTTER CONTROL SYNTHESIS METHODOLOGY

This section presents an overview of Honeywell's approach to synthesize active flutter controller for flexible vehicles. The main design objective is to increase the flutter free air speed by at least 20 percent (44 percent in dynamic pressure) at Mach number 0.9.

Honeywell's design procedure using LQG theory consists of three parts:

- Optimal state feedback synthesis
- Robust Kalman estimator synthesis
- Practicalization of the resulting optimal controller.

First, the flutter design model, for the DAST ARW1 wing, is described. This is followed by the step-by-step description of the design procedure to synthesize a practical flutter controller. A brief description of the software tool KONPACT II is given at the end of the section.

The Flutter Design Model

The flutter system consists of a half wing, an aileron, actuator, and a set of sensors. The basic modeling task is to obtain a state space representation for the flexible wing with unsteady aerodynamics (ref. 2). The modeling procedure is discussed in Section III. A block diagram of the overall flutter system is shown in Figure 1. The white noise input η_g , is shaped by the gust filter dynamics to produce the effect of gust (wind) force on the wing. The control input, u_c , moves the control surface through the actuator dynamics to control the fluttering of the wing. The output of the sensors is m_s .

The flutter design model

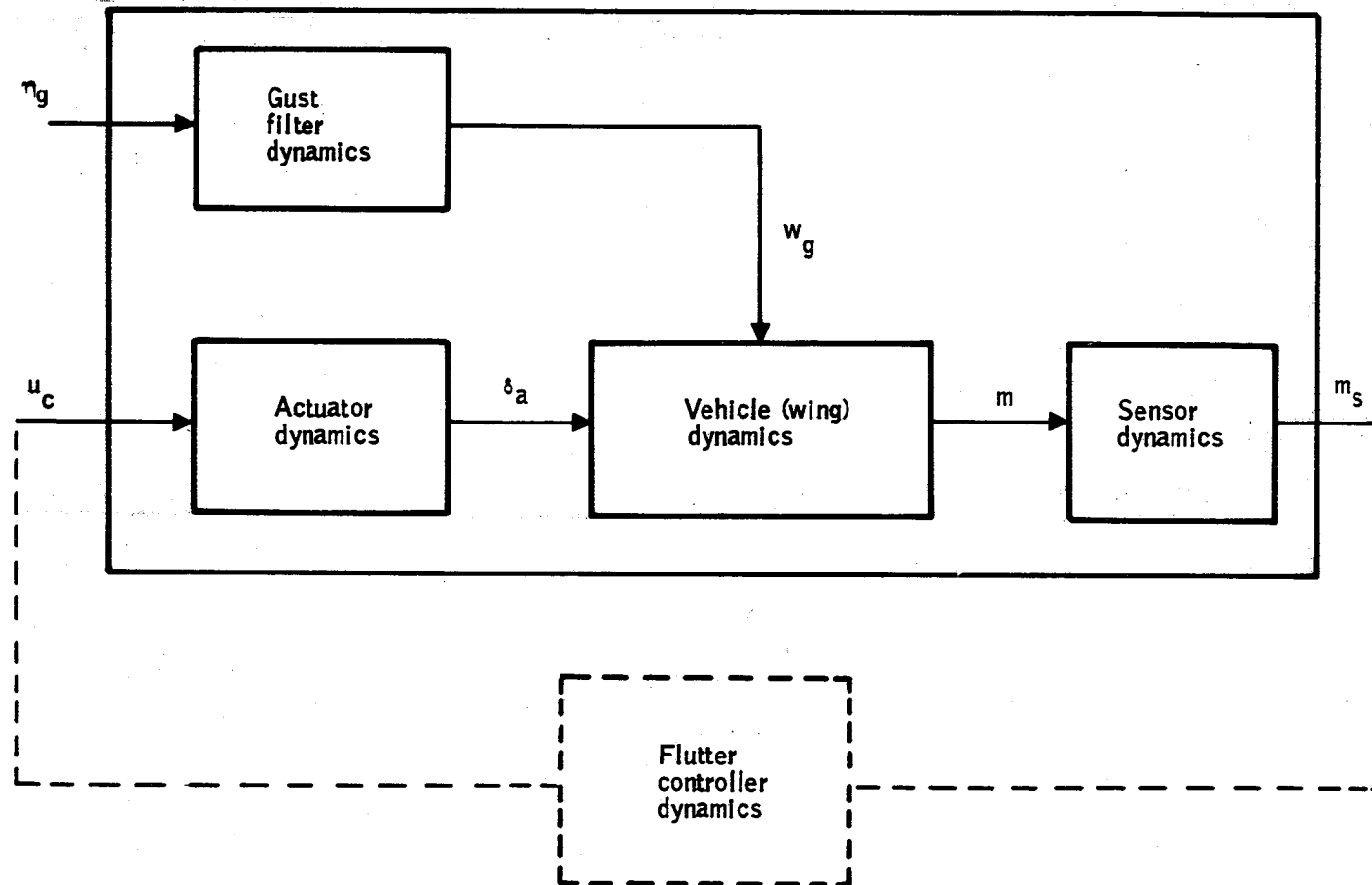


Figure 1. - Overall flutter system block diagram.

Optimal State Feedback Design

In this control synthesis step, it is assumed that all the states (x) of the flutter design model are available. The control law is obtained as a set of feedback gains. The optimal state feedback control law represents the best that is achievable. It is guaranteed by theory to have good robustness properties (ref. 3). As a more of the practical requirements are enforced, the performance of the overall system deteriorates. So the optimal state feedback control should be synthesized with stringent performance requirements. The details of this design procedure are the subject of Section IV.

Robust Kalman Estimator Design

This step eliminates the need to have all the states of the flutter design model. It is assumed that enough sensors are placed on the wing so that the states of the flutter design model can be estimated. The flutter control law is then obtained by multiplying the estimated states by optimal state feedback gains (obtained in the previous step). Here the designer has the freedom to choose the number and location of sensors. Also, there is freedom while designing the robust Kalman estimator to improve the robustness property of the overall system at the expense of rms performance. These issues are discussed in Section V.

Practicalization and Performance Analysis

The robust Kalman estimator together with the optimal state feedback gains constitute a flutter controller that is implementable. However, the cost and effort of implementation can be significantly improved by approximating the above flutter controller by a low-order one. The two procedures suitable for this task are residualization and frequency response matching

(ref. 4 and 5). Once the flutter controller is practicalized, it should be evaluated with a detailed performance analysis at various mach numbers and dynamic pressures to assure its operation throughout the flight envelope. The details of this design step are discussed in Section VI.

KONPACT II Software for Active Control Design

KONPACT software (ref. 1) was developed to automate the modeling and design steps of active control to minimize the error of data handling. The software uses advanced computational techniques to perform system modeling, modern control synthesis, analysis and design of active control systems. This software was updated with respect to modeling procedures and design methods developed during this study. The resulting software is called KONPACT II. Figure 2 shows the program organization, for more details on the software the reader is referred to Volume III.

KONPACT II

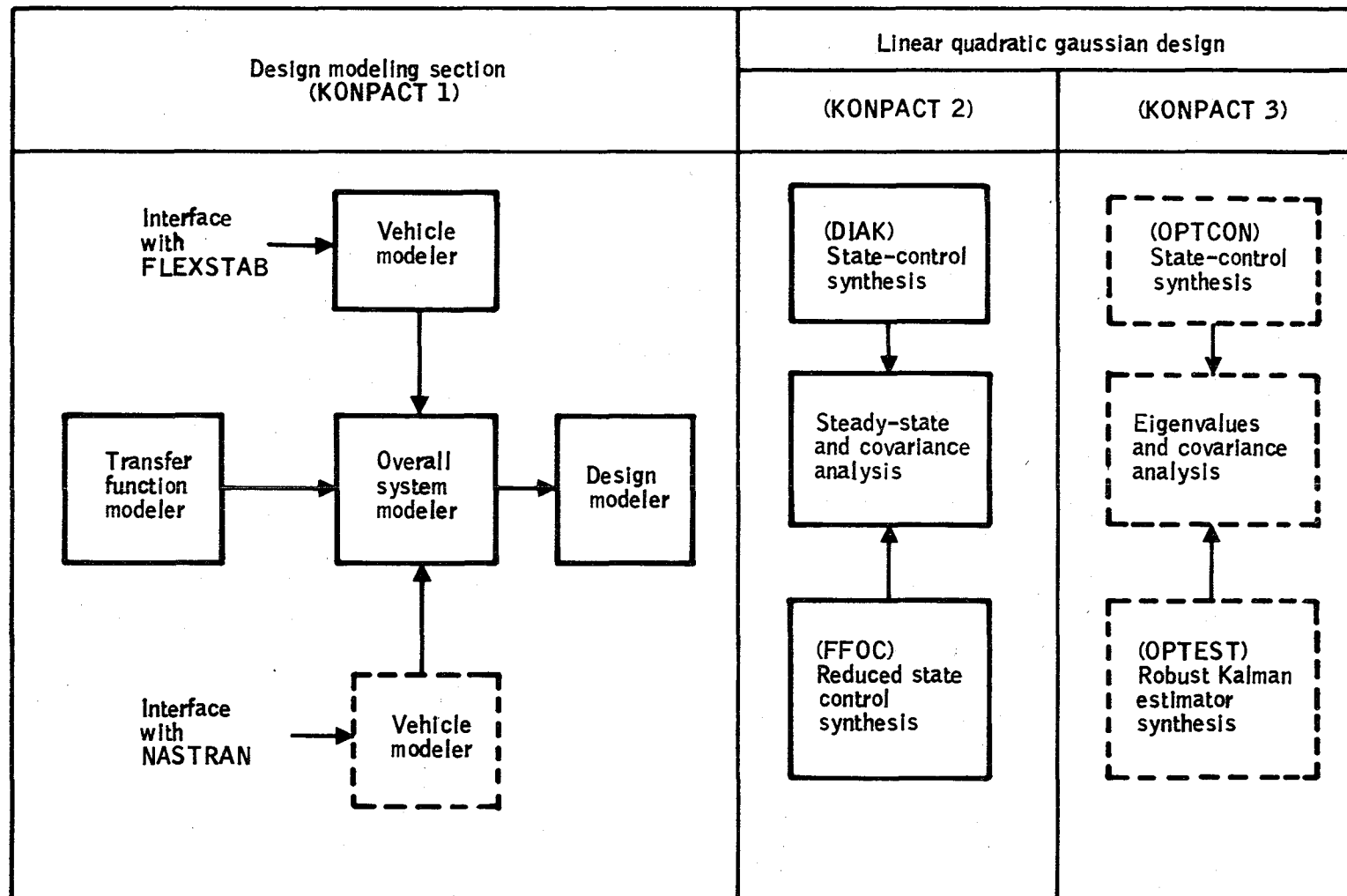


Figure 2. - Program organization of KONPACT II.

SECTION III

DYNAMIC MODELING FOR FLUTTER CONTROL DESIGN

The flutter system consists of a half wing, an aileron, actuator, and a set of sensors.

The wing is a dynamically scaled representation of a transport-type research wing. It is scaled to flutter within the operational limits of the NASA Langley transonic dynamic tunnel (TDT). It is provided with a hydraulically actuated trailing edge control surface. Figure 3 is the model geometry of the wing. It has an equivalent aspect ratio of 6.38 and a leading edge sweep of 44.32° . The trailing edge control surface is 20 percent of the local wing chord and is located between the 76.3 percent and 89.3 percent semispan stations.

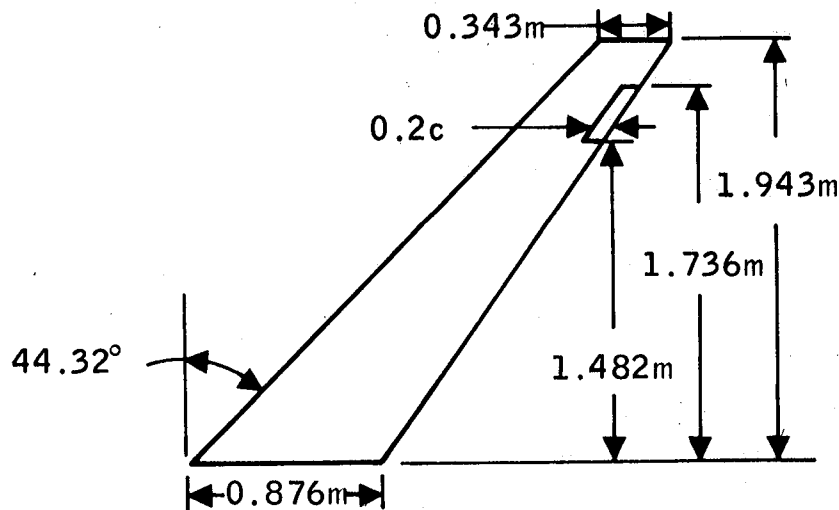


Figure 3.- Model geometry of the DAST ARW1 wing.

Modeling the Dynamics of the Wing and the Aileron

Using analysis technique described in (ref. 6) the equations of motion can be written as

$$(Ms^2 + K) \begin{pmatrix} \xi_F \\ \xi_C \end{pmatrix} + \bar{q} Q(k) \begin{pmatrix} \xi_F \\ \xi_C \\ \xi_G \end{pmatrix} = 0 \quad (1)$$

where

- ξ_F = Vector of generalized coordinates for flexible modes
- ξ_C = Vector of generalized coordinates for control surfaces
- ξ_G = Vector of generalized coordinates for gust inputs
- M = Generalized mass matrix
- K = Generalized stiffness matrix

$Q(k)$ is the unsteady aerodynamic influence coefficient matrix evaluated at various reduced frequencies k given by the expression

$$k = \frac{\omega c}{2V} \quad (2)$$

where

- ω = Circular frequency
- c = Reference chord length
- V = Velocity of the vehicle

and \bar{q} is the dynamic pressure and is given by the expression

$$\bar{q} = 1/2 \rho V^2 \quad (3)$$

where

- ρ = Density of air

For this study, NASA LaRC provided a NASTRAN finite element model of the wing. The first 10 elastic modes, generalized masses, and frequencies were provided. The modes cover a frequency range of 5.23 to 118.15 Hz. The unsteady aerodynamic influence coefficient matrix data was provided for eight reduced frequencies ranging from 0 to 1.2. The mode shape data at the various nodes of the finite element model was also provided to compute the sensor (accelerometer) output equations.

The state space flutter model is obtained by the least square approximation of the unsteady aerodynamic forces. This approximation has been shown to give accurate models for flutter analysis and design (ref. 6 and 7). The unsteady aerodynamic force matrix $Q(s)$ is approximated by a rational polynomial, in the Laplace transform variable s , given by

$$Q(s) \approx A_0 + A_1 \left(\frac{cs}{2V} \right) + A_2 \left(\frac{cs}{2V} \right)^2 + \sum_{m=1}^L \frac{D_m s}{\left(s + \frac{2V}{c} \hat{k}_m \right)} \quad (4)$$

where A_0 , A_1 , A_2 , D_m , $m = 1, L$ are the aerodynamic coefficient matrices and \hat{k}_m , $m = 1, L$ are the aerodynamic lags. The original form of this approximation was suggested by R. T. Jones (ref. 2).

The values of \hat{k}_m are selected, within the range of reduced frequencies over which $Q(k)$ has been calculated, to minimize the error of approximation. Usually only a few values of \hat{k}_m near the reduced flutter frequency are required. The aerodynamic coefficient matrices are computed by least-square fit of the aerodynamic force at k_i , $i = 1, N$. The least-square procedure and the conversion of the resulting s -plane approximation to state space description by using minimal realization technique is described in Appendix A (Volume II). Figure 4 is a block diagram of the state space realization of the flutter model. The root locus at mach number = 0.9 as the dynamic pressure is varied is given in Figure 5 (the flutter model has $L = 4$ and $\hat{k}_1 = 0.2$, $\hat{k}_2 = 0.4$, $\hat{k}_3 = 0.6$ and $\hat{k}_4 = 0.8$). Note that as the dynamic pressure is varied the frequencies of modes 1 and 2 tend to coalesce exhibiting a

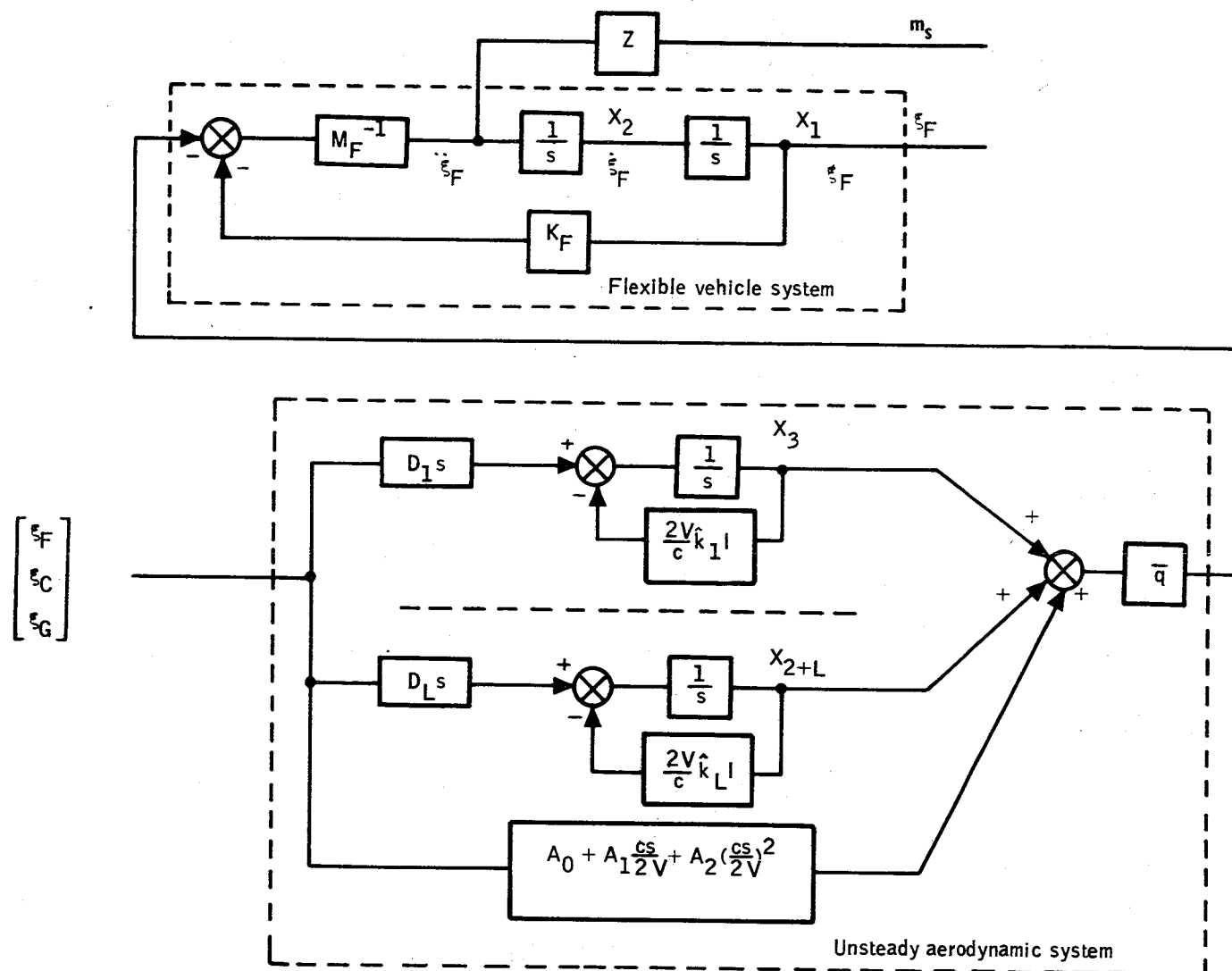


Figure 4. - State space realization of the flutter model.

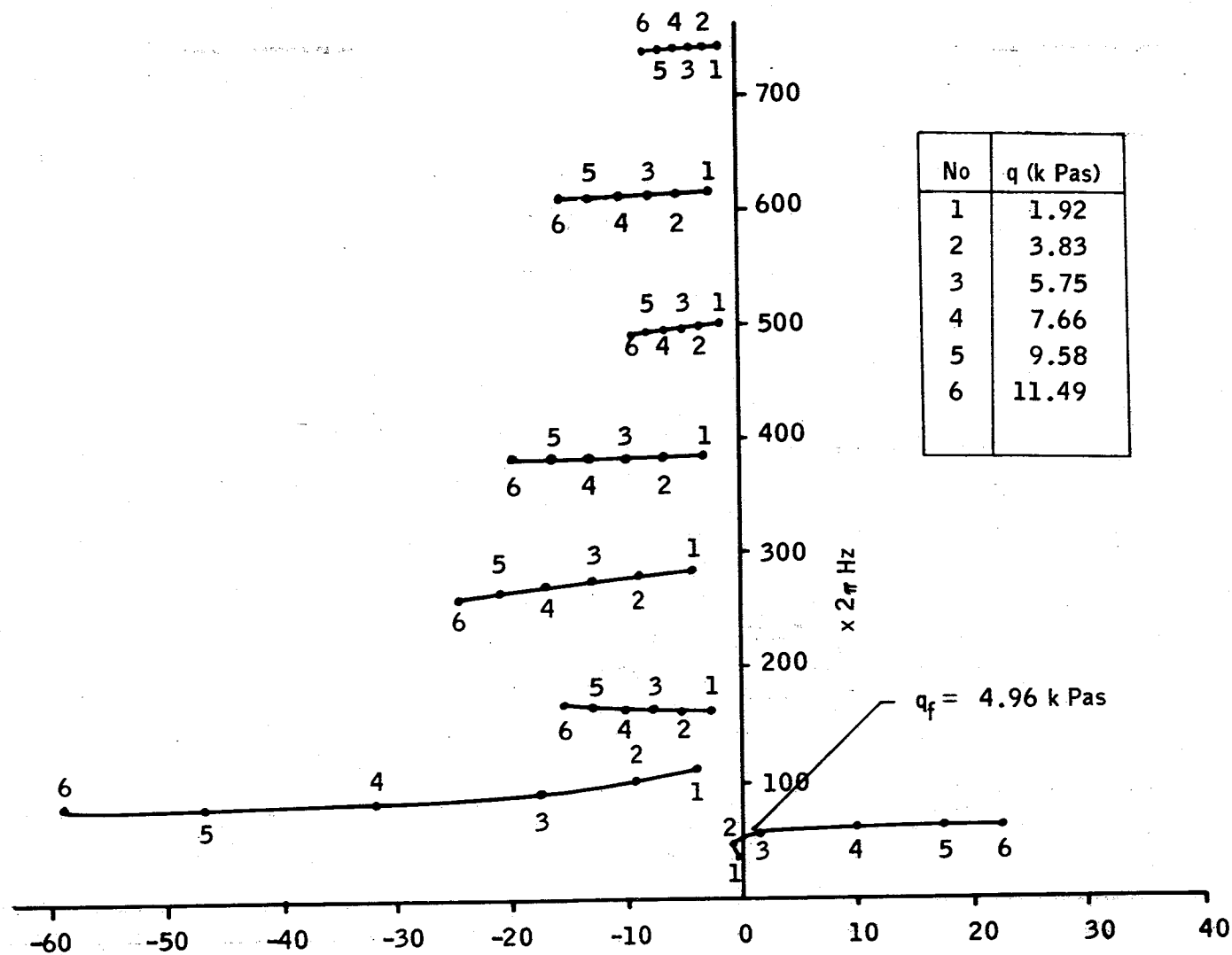


Figure 5.- Root locus at $M = 0.9$ (open loop).

typical bending - torsion type flutter behavior. The results are in agreement with the experimental flutter studies conducted by NASA in the Langley TDT (ref. 8).

The Actuator Dynamics

The trailing-edge control surface is driven by an electrohydraulic servo actuator system. If the aeroelastic effects and the mass of the aileron are neglected, the deflection of the actuator will be the same as that of the aileron. NASA measured the actuator transfer function experimentally during wind tunnel tests (ref. 9). The following transfer function approximates the measured transfer function:

$$\frac{\delta_a}{u_c} = \frac{1.915 \times 10^7}{(s + 214) (s^2 + 2 \times 0.1 \times 94.6 \times s + 94.6^2)} \quad (5)$$

where u_c is the control signal and δ_a is the control surface deflection. The aileron rate and acceleration are obtained by implementing the actuator dynamics given by equation (4) as shown in Figure 6.

Based on the maximum control surface displacement and rate, NASA specified the maximum RMS deflection and rate to be 4 deg and 250 deg/sec, respectively, for an RMS gust velocity of 0.3048 m/s. In addition, a control system frequency response attenuation boundary was specified to meet the actuator bandwidth requirement, Figure 7.

The Gust Model

The RMS control surface displacement and rate are determined by using a second-order Dryden wind model.

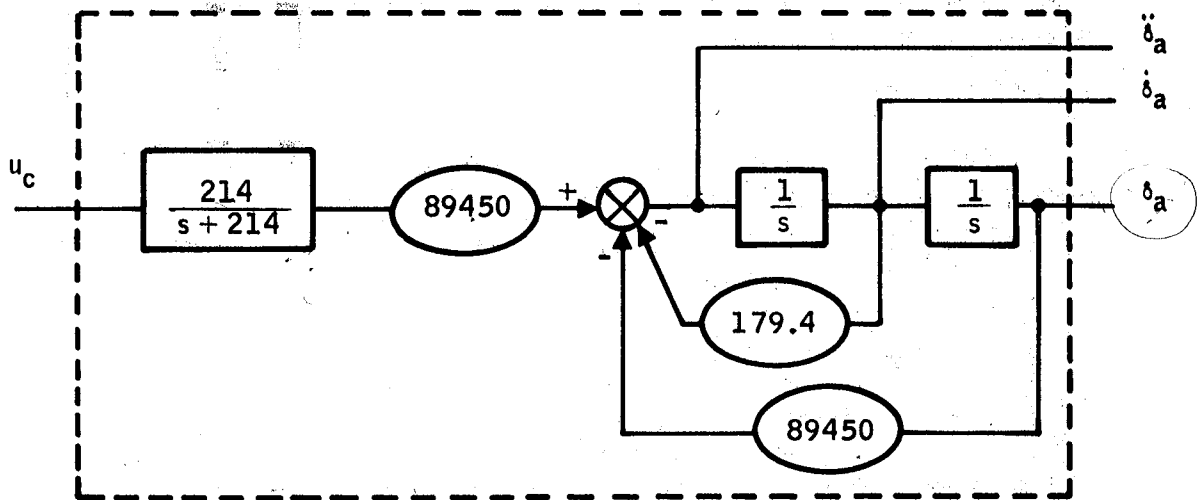


Figure 6. - Implementation of actuator dynamics.

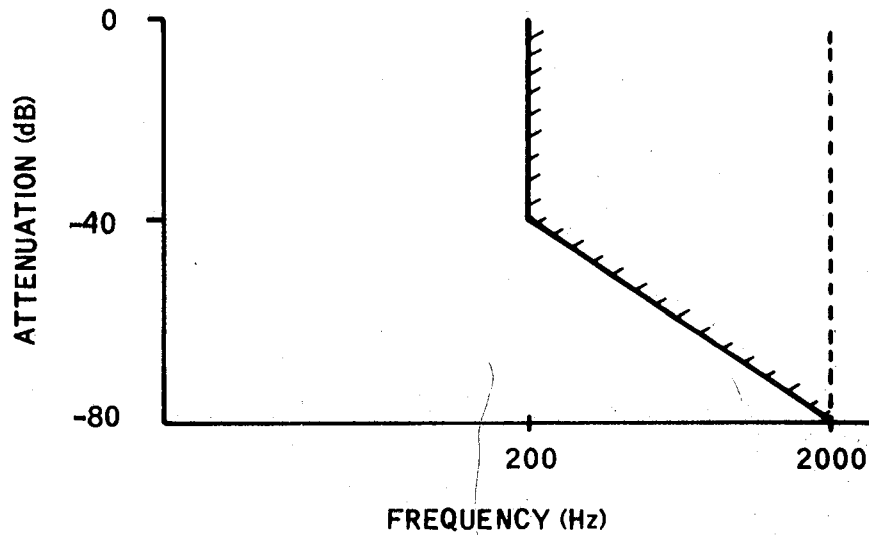


Figure 7. - Control system frequency response attenuation boundary.

The Von Karman power spectrum to describe the vertical component of one-dimensional atmospheric turbulence, (ref. 10) is

$$\phi_{\omega g}(\omega) = \frac{\sigma_{\omega g}^2 L}{\pi V} \frac{\left[1 + \frac{8}{3} \left(1.339 \frac{L\omega}{V}\right)^2\right]}{\left[1 + \left(1.339 \frac{L\omega}{V}\right)^2\right]^{11/16}} \quad (6)$$

where

$$\begin{aligned} L &= 30.48 \text{ m} \\ V &= 137.16 \text{ m/s} \\ \sigma_{\omega g} &= 0.3048 \text{ m/s} \end{aligned}$$

The second-order Dryden wind model to represent the Von Karman power spectrum (ref. 10) is

$$\frac{\omega_g}{\eta_g} = \frac{\sigma_{\omega g} \sqrt{\frac{L}{V}} \left(1 + \sqrt{3 \frac{L}{V}} s\right)}{\left(1 + \frac{L}{V} s\right)^2} \quad (7)$$

Substituting for L, V and $\sigma_{\omega g}$,

$$\frac{\omega_g}{\eta_g} = \frac{2.07 (s + 2.6)}{(s + 4.5)^2} \quad (8)$$

A first-order Dryden model is obtained by approximating equation (8) over the frequency range from 0 to 100 rad/sec. It is given by the transfer function

$$\frac{\omega_g}{\eta_g} = \frac{2.5926}{(s + 3.3607)} \quad (9)$$

The two wind models over the frequency range of interest are compared in Figure 8.

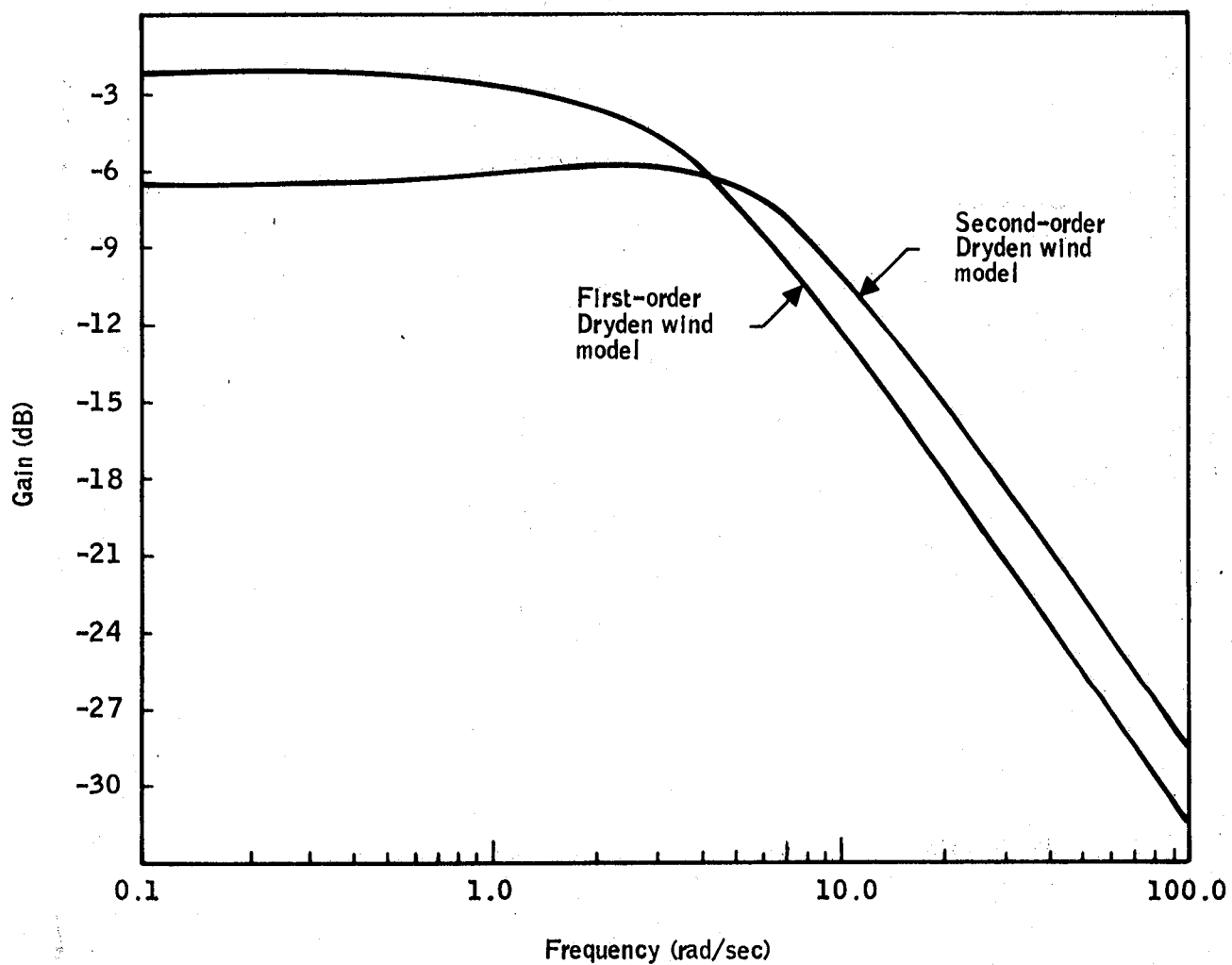


Figure 8. - Comparison of two dryden wind models.

The Design Model

The design model is obtained by combining the wing, the actuator and the gust model and defining the design responses for LQG design (ref. 4). Figure 9 is a block diagram of the design model. The requirement on the design model is that it should be of as small an order as possible so that the design costs are reduced. Residualization is a reduction procedure well-suited to approximate the high-frequency modes (ref. 4). In the case of the flutter model, the parameter L , which denotes the number of aerodynamic lag terms, provides another natural procedure for reduction of order of the design model. In this study, a reduced-order design model was obtained by retaining modes 1, 2, 4, 5 and 6 and using $L = 1$. The order of this design model is 20 states. This reduced-order model preserves the open-loop flutter characteristic to within 5 percent. For the final performance analysis, a model was obtained using modes 1, 2, 4, 5, 6, 7, 9 and 10 and using $L = 4$. The order of this model is 53 states. The results presented in Section VI show that the performance values are within 15 percent. The reduction in the design cost is quite significant.

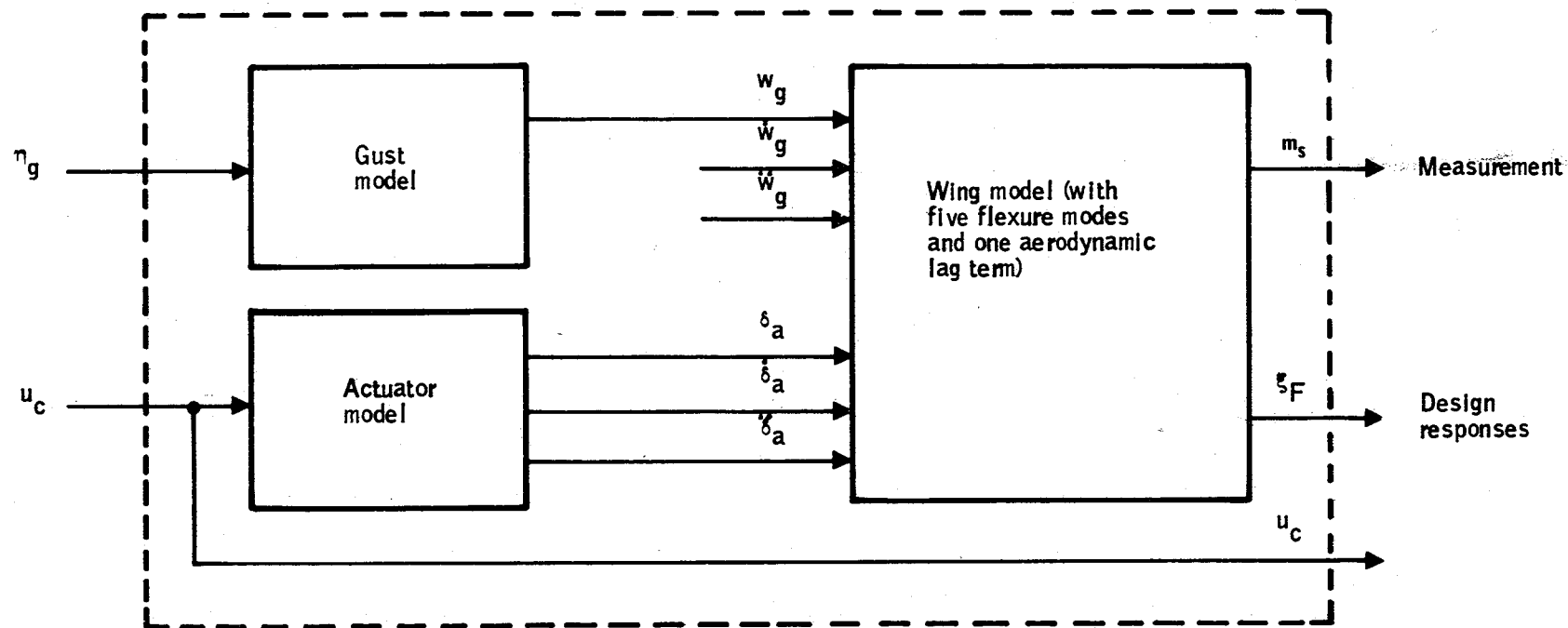


Figure 9. - Block diagram of the design model.

SECTION IV

OPTIMAL STATE FEEDBACK DESIGN AND CONTROL SURFACE OPTIMIZATION

Optimal state feedback synthesis is the first step in the active control design methodology to obtain practical control laws. Three sets of results are presented for this step in this section. They are:

- State feedback design
- Control surface optimization, and
- Insensitive design

In addition, the results of control-observe-ability are also presented.

The state feedback design results with nominal control surface are presented first. They show the best performance achievable at the design condition. Both first-order and second-order Dryden wind models are used. The second-order wind model enforces response values that are 40 percent larger. Fifteen controllers (two with a first-order wind) are synthesized, all controllers meet performance requirements, one with each wind model is chosen for subsequent design efforts.

The results of two control surface optimization problems are presented next. For the first, the aileron position is optimized over those with a semi-span of 0.130 (the same as the nominal). For the second, the optimization is for any semi-span within the allowable range of 0.660 and 0.937 of semi-span. For the first case, the best aileron position is as far out-board as possible. Reduction of RMS values of aileron deflection and rate of 3.21 and 1.73 percent are achieved. For the second case, the best aileron is that for maximum semi-span. Reductions of RMS values of aileron deflection and rate of 45.93 and 48.91 percent are achieved.

Insensitive design results are then presented. The uncertainty weighting procedure is used to develop constant controllers that provide good control in spite of large variations in model coefficients that are a function of dynamic pressure. The price paid is a small increase in RMS response activity.

Finally, an assessment procedure for the quality of controllability and observability is discussed. It is better than the rank test. The quality of controllability is reasonably well graded. The theory is also applied to accelerometer placement and is found to be of value.

State-Feedback Design

The performance objective is to stabilize the wing in the flutter condition at 0.9 Mach and a dynamic pressure of 7.66 k Pa. The final controller should have RMS response values for aileron (δ) and aileron rate ($\dot{\delta}$) less than 4 deg and 250 deg/s for an RMS wind of 0.3048 m/s. At the full-state feedback design step the control activity should be about 35 percent smaller to allow for the performance deterioration at the subsequent design steps.

The plant model is:

$$\dot{\mathbf{x}} = \mathbf{Ax} + \mathbf{B}_1 \mathbf{u} + \mathbf{B}_2 \boldsymbol{\eta} \quad (10)$$

$$\mathbf{r} = \mathbf{Cx} + \mathbf{Du} \quad (11)$$

where

$\mathbf{x}_i = \boldsymbol{\eta}_i$ ($i = 1, 5$) flexure mode deflections in m

$\mathbf{x}_i = \dot{\boldsymbol{\eta}}_{i-5}$ ($i = 6, 10$) flexure mode rates in m/s

\mathbf{x}_i ($i = 11, 15$) unsteady aerodynamic states

x_i ($i = 16, 18$) actuator states

$x_{16} = \delta$ Aileron deflection in deg

$x_{17} = \dot{\delta}$ Aileron rate in deg/s

$x_{last} =$ Wind gust velocity (scaled for 0.3048 m/s)

$u =$ Scalar control input

$\eta =$ Unit white noise

The model is of 19-order or 20-order depending on whether the first-order or second-order (Dryden) wind model is used.

The full-state feedback control law

$$u = Kx \quad (12)$$

is determined from

$$J = \min_u E\{r' Q r\} = \min_u E\{x' \tilde{Q} x + \rho u^2\} \quad (13)$$

We present two sets of results with the first order wind model: Sirisena method and baseline.

With the Sirisena (ref. 11) a response transfer function r/u is constructed by deleting the wind and requiring the real parts of the zeros to be $-1.01*$ (open-loop poles; except the first-order actuator pole).

Then

$$r/u = c' x/u \quad (14)$$

$$\tilde{Q} = cc' \quad (15)$$

As $p \rightarrow 0$, the closed-loop poles approach the numerator zeros, and the actuator pole goes to $-\infty$; the wind state remains invariant. Experience shows the desired asymptotic properties of this "minimally acceptable" feedback controller are achieved at nonzero values of ρ with acceptable values of pole position. Volume II has \tilde{Q} and ρ values.

Table 1, column case 0, lists the nonzero diagonal elements of the weighing matrix Q for the baseline case. Columns S and 0 show that both the Sirisena and baseline cases have highly acceptable RMS responses with the Sirisena being slightly better. Actuator pole positions are essentially at their open-loop value; the Sirisena real pole is slightly stiffer. Both are viable candidates for further development but we will subsequently (Sections V and VI) use only the baseline.

Figure 10 shows that both the Baseline and Sirisena controllers provide effective stabilization over a dynamic pressure range from 3.83 to 8.62 k Pa (at Mach 0.9).

Columns 1-13 of Table 1 present results with the second-order Dryden wind model. Cases 0 and 2 use the same quadratic weights; the RMS responses are 40 percent greater with the second-order wind model.

For case 3 there is weight only on control. Kwakernack and Sivan (ref. 12) show this is also a "minimally acceptable" optimal control; it reflects the unstable poles.

For cases 1-5 there are no weights on δ or $\dot{\delta}$. Actuator poles are near their open-loop values but RMS response values (particularly for aileron rate) are too close to their limit values. We therefore weighted δ and/or $\dot{\delta}$ in cases 6-13 to reduce RMS control responses. We select case 8 as a baseline for further design effort.

TABLE 1. - STATE SYNTHESIS SUMMARY

Case		⑤ ^a	⑥ ^a	⑦	⑧	⑨	⑩	⑪	⑫	⑬	⑭	⑮	⑯	⑰	⑱	
Quadratic weights	1		q**	q	q	0	q	q	q	q	q	q	q	0	0	0
	2		q	q	q	0	q	q	q	q	q	q	q	0	0	0
	3		q	q	q	0	q	0	q	q	q	q	q	0	0	0
	4		q	q	q	0	q	0	q	q	q	q	q	0	0	0
	5		q	q	q	0	q	0	q	q	q	q	q	0	0	0
	6		0	0	0	0	0	0	5 000	0	0	0	5 000	5 000	0	0
u		50 000	5 000	50 000	50 000	500 000	500 000	500 000	50 000	50 000	50 000	50 000	50 000	500 000	50 000	
RMS response	f	1.788	1.804	3.168	2.548	2.492	2.492	2.505	2.559	2.579	2.704	2.683	2.628	2.641	2.526	
	u	151.4	164.9	249.4	229.5	218.0	249.2	220.0	195.7	200.4	189.4	168.0	169.0	169.6	168.8	186.4
	u		1.845	3.263	2.604	2.534	2.536	2.536	2.549	2.612	2.630	2.748	2.730	2.568	2.679	2.567
Cost	J		0.2384 × 10 ⁶	0.1323 × 10 ⁶	0.4702 × 10 ⁶	0.3210 × 10 ⁶	0.3384 × 10 ⁷	0.3380 × 10 ⁷	0.3835 × 10 ⁷	0.5151 × 10 ⁶	0.5529 × 10 ⁶	0.7985 × 10 ⁶	0.8349 × 10 ⁶	0.6783 × 10 ⁶	0.8436 × 10 ⁶	0.3989 × 10 ⁶
Actuator poles	Real	-221.5	-212.5	-194.1	-212.5	-214.8	-213.8	-213.9	-172.0	-162.9	-138.6	-90.34	-90.39	-90.04	-90.04	-141.3
	frequency	47.60	47.76	48.99	47.76	47.60	47.62	47.62	53.21	53.17	58.57	83.30	83.32	83.33	83.32	58.58
	damping	0.3000	0.2994	0.2970	0.2994	0.2999	0.2999	0.2999	0.2999	0.4558	0.4550	0.5280	0.6352	0.6349	0.6349	0.5265

* Sirisena design

* With a first-order wind model

** q = 0.5088*7

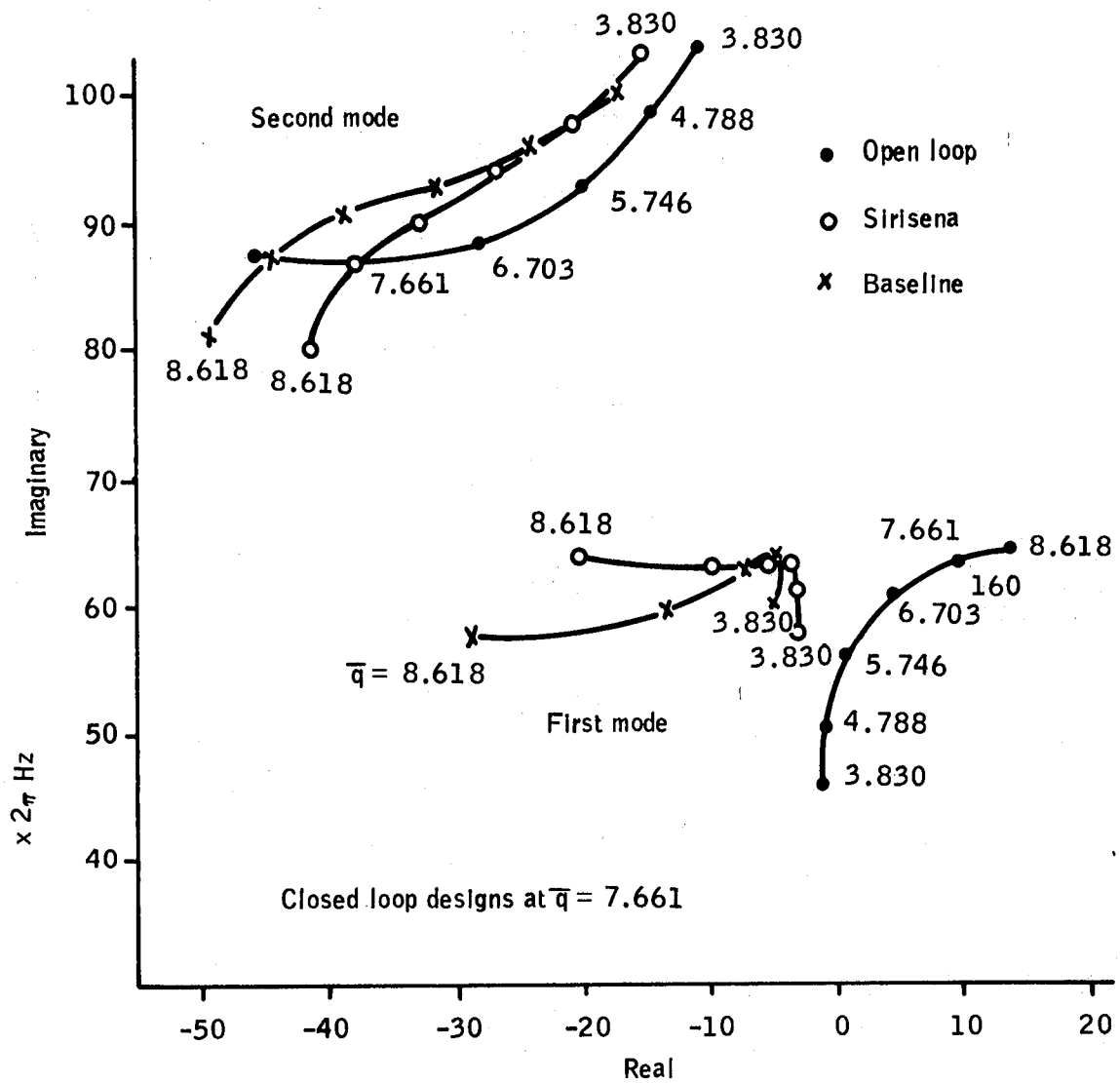


Figure 10. - Sirisena and baseline loci.

As is usual in the application of LQG methodology, we find here that its ease of use in providing tradeoff data to justify its use. In the present synthesis process, it is also the first step in the synthesis of practical controllers.

Control Surface Optimization

Given a scalar y of control surface positions, we wish to determine the optimal value of y and the feedback gain matrix K .

$$u = Kx \quad (16)$$

to perform

$$J = \min_y \min_u E \{r' Q r\} \quad (17)$$

and Q is given by the case 8 values of Table 1. We use a modification of the Johnson algorithm (ref. 13) as is discussed in Appendix F of Volume II.

To determine the optimal control surface position we start with an initial y and successively perturb y to get reductions in J until a minimum is achieved. Because of strong monotonicity, y is simply incremented to the boundary; we do compute the one-sided difference approximation to the gradient of equation (17) to be assured that we do not skip over a local minimum.

Table 2 summarizes the results. The first row entry is with the nominal aileron and is the same as case 8 of Table 1. Row 3 is with the same aileron position but employs a polynomial fit model for the aileron aerodynamic data. There are small unimportant differences.

Rows 2-5 establish that for ailerons whose span is 0.130 of the wing semispan that the most outboard allowable position is best. Our first itera-

TABLE 2. - CONTROL SURFACE POSITION OPTIMIZATION

Aileron position		Poly-nominal fit		RMS		J	DJ _{ij}	i	j	
Part of semispan			δ	$\dot{\delta}$	u					
Inboard	Outboard		Deg	Deg/sec						
0.763	0.893	No	2.579	189.4	2.638	0.5529 x 10 ⁶	-			1
0.753	0.883	Yes	2.620	192.0	2.671	0.5668 x 10 ⁶	0.9047 x 10 ⁴	3	2	2
0.763	0.893	Yes	2.594	190.5	2.644	0.5576 x 10 ⁶	-			3
0.783	0.913	Yes	2.584	188.5	2.599	0.5438 x 10 ⁶	-0.1434 x 10 ⁵	3	4	4
0.807	0.937	Yes	2.510	187.2	2.561	0.5338 x 10 ⁶	-0.2582 x 10 ⁶	3	5	5
0.730	0.937	Yes	1.717	124.2	1.756	0.2981 x 10 ⁶	0.5753 x 10 ⁷	7	6	6
0.660	0.937	Yes	1.428	97.7	1.462	0.2308 x 10 ⁶	-0.8458 x 10 ⁸	6	7	7

tion (row 2) was to move the aileron inboard, δ , $\dot{\delta}$, u , and J all increased. The one-sided difference is an excellent approximation to the differences in the values of J . This assures us of monotonicity over inboard shifts in aileron by increments of less than 0.01 semispan and assures us reasonably well that inboard shifts are undesirable.

We then moved the aileron outboard from its nominal position in two steps (rows 4 and 5) to the maximum allowable. The values of δ , $\dot{\delta}$, u , and J are monotone decreasing and DJ 's are again a good approximation to the changes in J . It is clear that the outboard aileron position is optimum among those whose span is 0.130 of the wing semispan. The improvements over the nominal position are less than 5 percent.

The previous results indicate the aileron should be as far outboard as possible. If further improvements are desirable it is necessary to increase the aileron span. We held the outboard position at its maximum value and examined increasing the aileron span by moving the aileron inboard position further inboard to the inboard extreme. We did this in two steps-rows 6 and 7. The values of δ , $\dot{\delta}$, u , and J are decreased by about 45 percent.

There are no adverse side effects of using this optimum surface placement solution on this unflapped vehicle. We established this by looking at the roots, gains, and RMS responses.

Insensitive Design

Given a dynamic pressure (\bar{q}) dependent model

$$\dot{\mathbf{x}} = \mathbf{A}(\bar{q}) \mathbf{x} + \mathbf{B}_1 u + \mathbf{B}_2 \eta \quad (18)$$

we want to determine a constant full-state feedback control matrix \mathbf{K} that enforces good performance over a large dynamic pressure range. We use the uncertainty weighting procedure (ref. 14). We use a weighting matrix

$$\bar{Q} = Q + \lambda (\delta A)' (\delta A) \quad (19)$$

where

$$\delta A = A(\bar{q}) - A(\bar{q}_0) \quad (20)$$

\bar{q}_0 = Design dynamic pressure

\bar{q} = An off-design dynamic pressure

λ = Control designers insensitivity parameter

For this application, the design model was obtained by retaining only the first two flexure modes, the third-order actuator and the first-order approximation to the Dryden wind model. The matrix Q was taken as the case 0 matrix of Table 1. Design and off-design values of \bar{q}_0 and \bar{q} are taken both at 5.27 and 7.66 k Pa ; they were also taken at 7.66 and 5.27 k Pa. We determined that a good value for λ is 0.1. This is the minimum value of λ that yields about all of insensitivity achievable.

Baseline and insensitive controllers were designed for two nominal values of dynamic pressure $\bar{q}_0 = 5.27$ k Pa and $\bar{q}_0 = 7.66$ k Pa. The performance of the insensitive controllers was compared with that of the nominal controllers as the dynamic pressure was varied. Performance evaluations were based on comparing eigenvalues and RMS responses as dynamic pressure was varied between 5.27 k Pa and 7.66 k Pa.

For the designs (baseline and insensitive) developed for 7.66 k Pa , performance was evaluated as dynamic pressure was reduced to 5.27 k Pa. The response produced by the insensitive controller showed a slightly smaller variation with dynamic pressure than the baseline controller but the reduction in sensitivity was not significant. The baseline controller produced responses which did not vary a great deal with dynamic pressure and it was difficult to improve upon this performance.

For the designs developed for 5.27 k Pa , performance was evaluated as dynamic pressure was increased to 7.66 k Pa. In this case the baseline controller went unstable at approximately 5.98 k Pa ; whereas, the insensitive control was stable up to 7.66 k Pa. Furthermore, the RMS values of control surface displacement and velocity did not greatly exceed the allowable values at the higher values of dynamic pressure. In this case the insensitive controller was clearly superior to the baseline controller.

Control-Observe-Ability

In the following the quality of controllability and observability are discussed pertaining to the control surface/sensor placement problem. The procedure given is due to R. G. Brown (ref. 15).

Given the nth order system

$$\dot{x} = Ax + Bu \quad (21)$$

$$r = Mx$$

The controllability and the observability matrices are given by

$$CM = \left[A^{n-1}B \mid A^{n-2}B \mid \dots \mid AB \mid B \right] \quad (22)$$

$$OM = \left[\left(A^T \right)^{n-1} M^T \mid \left(A^T \right)^{n-2} M^T \mid \dots \mid A^T M^T \mid M^T \right]$$

Notation: OMCC is CM or OM with columns normalized by normalizing as CM or OM is being formed. The magnitudes of the elements of OMCC are within the limits of the computer word length and hence produces more accuracy. For example, given the k^{th} stage of computation OMCC of CM, the $(k+1)^{st}$ stage is calculated as follows:

$$\text{OMCC}_k = \left[O \mid \text{---} \mid \overline{A^{k-1}B} \mid \overline{A^{k-2}B} \mid \text{----} \mid \overline{B} \right] \quad (23)$$

$$\text{OMCC}_{k+1/2} = \left[O \mid \text{---} \mid \overline{A A^{k-1}B} \mid \overline{A^{k-1}B} \mid \overline{A^{k-2}B} \mid \text{--} \mid \overline{B} \right]$$

$$\text{OMCC}_{k+1} = \left[O \mid \text{---} \mid \overline{A^k B} \mid \overline{A^{k-1}B} \mid \text{-----} \mid \overline{B} \right]$$

where the overscore bar indicates column normalization. The m column vectors of OMCC are denoted as v_i and since OMCC is normalized, v_i are unit vectors and $v_i \in \mathbb{R}^n$. Now consider these m unit (Euclidian) n -vectors v_i ($n \leq m$) placed in an n by m matrix OMCC

$$\text{OMCC} = \begin{bmatrix} v_1 & v_2 & \cdots & v_m \end{bmatrix} \quad (24)$$

We seek n unit n -vectors u_j that extremize the cost function

$$L = \left(v_1^T u_j \right)^2 + \left(v_2^T u_j \right)^2 + \dots \quad (25)$$

Result 1. If u is any unit vector, $L(u)$ is cost in the direction u . If $\{u_j\}$ are an orthonormal basis, then

$$\sum_{j=1}^n L(u_j) = m \quad (26)$$

The extremizing unit vectors u_j form an orthonormal basis and are the eigenvectors of matrix OMDD where

$$\text{OMDD} = \text{OMCC} * \text{OMCC}^T \quad (27)$$

Result 2. The associated eigenvalues λ_j are the "costs" in the direction u_j

$$L_j = u_j^T * OMDD * u_j = \lambda_j \quad (28)$$

$$\lambda_j \geq 0 \quad (29)$$

$$\sum_{j=1}^n \lambda_j = m \quad (30)$$

If $L_j(u_j) = 0.$, u_j is nearly orthogonal to the vectors of OMCC. For unit vectors u_j such that $L_j(u_j) \geq 1.$, the vectors of OMCC span u_j with high quality.

To use these results to evaluate the quality of controllability or observability we calculate the controllability or observability matrices, normalize the columns and calculate the eigenvectors and eigenvalues of the OMDD matrix. We found the assessment to be superior to the rank test but deficient in shading the quality of control-observe-ability.

The above results can also be used to assess the quality of a prescribed accelerometer complement for spanning an open-loop mode acceleration subspace. We computed how well two accelerometers span the subspace of the first two acceleration modes. The best results are presented in Table 3; accelerometers at node points 16 and 57 are best. In Section V we will also show, using another criterion, that this is an effective choice.

TABLE 3. - BEST TWO ACCELEROMETERS FOR TWO MODES

Minimum eigenvalue	Accelerometer node points	
0.999	16	57
0.910	16	45
0.718	16	30
0.694	28	57
0.611	28	45
0.526	16	18
0.462	16	55
0.439	28	30
0.300	16	43

SECTION V

ROBUST KALMAN ESTIMATOR DESIGN AND SENSOR OPTIMIZATION

With full-state feedback the system is unconditionally stable, has good gain and phase margins, and has low bandwidth. As predicted by Doyle (ref. 16) with the ordinary Kalman estimator the system is conditionally stable, has poor gain and phase margins, and has high bandwidth. A procedure due to Doyle and Stein (ref. 17) is presented to synthesize robust Kalman estimators. This procedure permits compromising RMS response activity against robustness. Here robustness is characterized as gain and phase margins. If the sensor complement is minimum phase under control gains, full-state stability characteristics can be asymptotically achieved. The results of robust Kalman estimator design are presented for three sets of sensor complements. Three levels of robustness are used for each of the sensor complements and the results compared with that of ordinary Kalman estimators.

An optimization procedure, similar to the one employed in Section IV for control surface placement, is used to determine sensor locations that minimize the cost and RMS activity. Improvements of 15 percent in RMS responses are obtained.

Finally, the sensor position procedure of Stein and Harvey (ref. 18) is modified and applied. This yields the same sensor complement previously determined by control-observe-ability considerations.

Robust Kalman Estimator Design

As described in (ref. 17), the robust estimator design is obtained by adding an extra process noise directly to the control input of the plant during the estimator design.

The equations of motion are given by:

$$\dot{x} = Ax + B_1 u + B_1 \eta_c + B_2 \eta_g \quad (31)$$

$$m = Mx + \eta_m \quad (32)$$

Here η_g and η_m are the nominal gust and measurement noise with

$$E \{ \eta_g(t) \eta_g'(\tau) \} = W_g \delta(t - \tau) \quad (33)$$

$$E \{ \eta_m(t) \eta_m'(\tau) \} = W_m \delta(t - \tau) \quad (34)$$

and η_c is the additional process noise added at the control input with

$$E \{ \eta_c(t) \eta_c'(\tau) \} = q W_c \delta(t - \tau) \quad (35)$$

and q is the non-negative robustness parameter.

The robust estimator dynamics is given by:

$$\dot{\hat{x}} = A\hat{x} + B_1 u + L (M\hat{x} - m) \quad (36)$$

The robust estimator gain is given by:

$$L = -P_e M' W_m^{-1} \quad (37)$$

The error covariance matrix, P_e , is the solution of the Ricatti equation:

$$\begin{aligned} (A + LM)P_e + P_e(A + LM)' + L W_m L' \\ + B_2 W_g B_2' + q B_1 W_c B_1' = 0 \end{aligned} \quad (38)$$

For $q = 0$, we get the ordinary Kalman estimator design and as q is increased the estimator design becomes more and more robust and approaches the stability characteristics of the full-state feedback design.

The control u is given by

$$u = K\hat{x} \quad (39)$$

where the gain matrix K is obtained from the baseline case 0 of Table 1 (with first-order wind model).

Results for three sets of sensors are presented. In the first set, two accelerometers are used; one each at node points 16 and 57; this choice was determined by the control-observe-ability considerations in Section IV. For the second and third sets, single accelerometers are used at node points 18 and 28, respectively.

Ordinary Kalman estimators ($q = 0$ in equation (8)) were synthesized and the performance is summarized in Table 4. Row 1 presents the results with full-state feedback control; rows 2, 6, and 10 present the results with the three different sensor complements.

The values of RMS responses are modestly larger when Kalman estimators are used. The increases in δ are 29, 32, and 45 percent, respectively; $\dot{\delta}$ increases by 13, 20, and 18 percent, respectively. From this we see the first (two sensor complement) is best and that the second (node point 18) is preferable to the third (node point 28). All of them comfortably meet the objectives of 4 deg and 250 deg/sec for δ and $\dot{\delta}$.

The gain and phase margins of full state feedback control are guaranteed by Safanov and Athans (ref. 19); -6 dB and $+\infty$ dB in gain and ± 60 deg in phase. Row 1 shows that we comfortably exceed these values. The S(full-state feedback curve) of the Nyquist plot of Figure 11 shows the superlative stability characteristics.

TABLE 4. - ROBUSTNESS SUMMARY

Control	Sensor	q	RMS		Gain margin				Phase margin				Bandwidth
			δ	$\dot{\delta}$									
			Deg	Deg/sec	dB	Hz	dB	Hz	Deg	Hz	Deg	Hz	Hz
State	State	0.0	1.804	164.9	-8.1	9.90	∞	---	-63.7	7.05	+82.3	15.25	23.2
Kalman	16,57	0.0	2.330	186.2	-5.3	10.28	+ 6.4	21.87	-42.5	8.26	+32.4	13.64	59.8
Robust	16,57	0.000001	2.733	196.8	-6.6	9.85	20.0	75.28	-45.4	7.46	+66.2	13.56	19.3
Robust	16,57	0.00001	3.066	212.0	-7.3	9.87	21.5	103.56	-53.3	7.23	+72.9	14.23	11.1
Robust	16,57	0.0001	3.534	240.2	-7.7	9.90	24.9	149.65	-57.9	7.16	+76.3	14.64	21.8
Kalman	18	0.0	2.383	197.9	-3.9	10.49	+ 3.0	17.1	-43.9	8.71	+18.3	13.15	44.9
Robust	18	0.000001	4.018	158.5	-4.5	9.82	+ 8.4	4.84	-29.1	7.97	+43.9	12.21	15.3
Robust	18	0.00001	6.445	197.4	-5.6	9.72	+ 7.7	3.95	-34.3	7.48	+58.2	12.62	16.6
Robust	18	0.0001	11.534	243.4	-6.3	9.74	+ 7.9	3.01	-40.5	7.21	+65.6	13.10	17.8
Kalman	28	0.0	2.607	194.3	-1.8	61.20	+ 3.7	18.54	-41.5	8.55	+22.8	13.62	64.6
Robust	28	0.000001	3.781	164.6	-5.6	4.85	+26.3	2.21	-37.9	7.81	+55.6	12.75	16.7
Robust	28	0.00001	5.069	188.2	-6.8	9.80	+28.9	1.56	-46.2	7.31	+71.1	13.67	18.5
Robust	28	0.0001	6.998	204.7	-7.5	9.85	+50.7	0.37	-55.2	7.10	+76.6	14.42	21.2

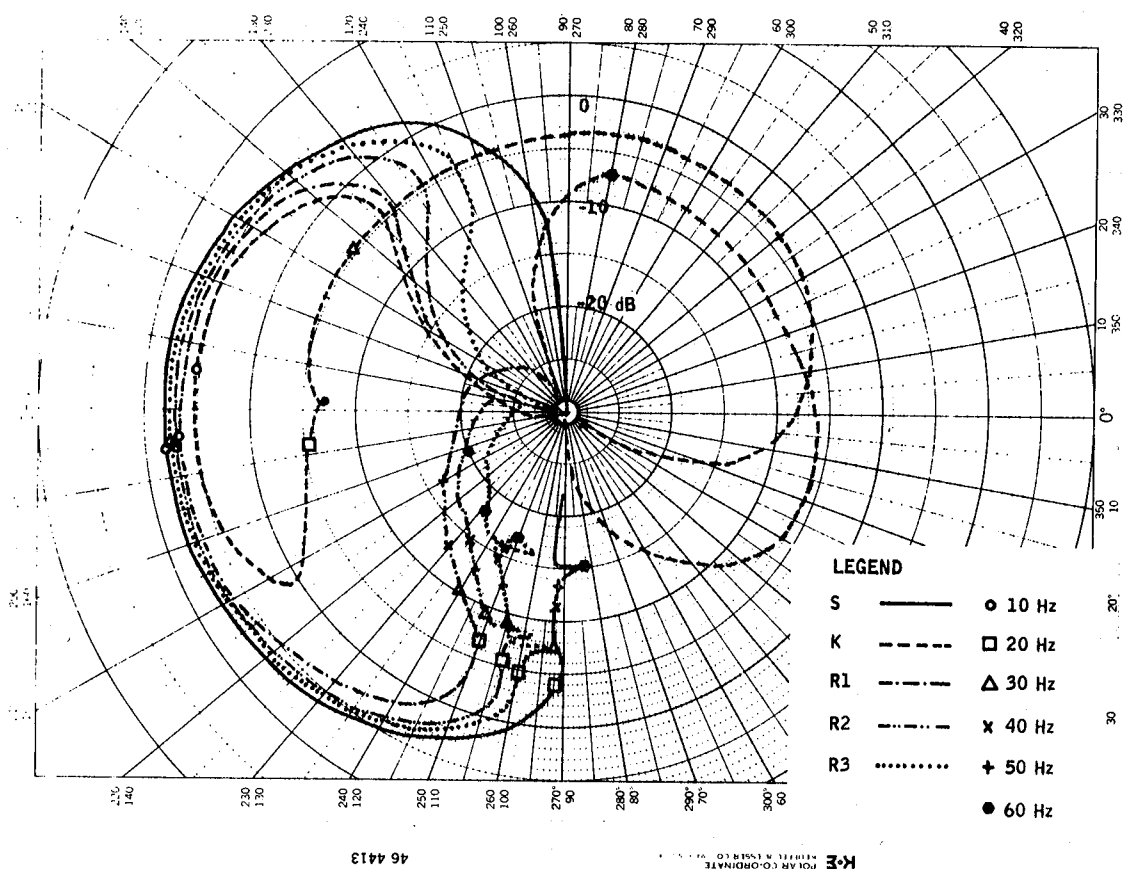


Figure 11. - Nyquist plot for nodes 16, 57.

As predicted by the work of Doyle (ref. 16), Table 4 shows that with ordinary Kalman estimators the magnitudes of negative stability margins are less than 6 dB and phase margin magnitudes are less than 60 deg. The K (Kalman) curves of Figures 11-13 demonstrate the poor stability characteristics.

Though not directly addressed by theory, it is interesting to note bandwidths. We define the bandwidth as the highest frequency at which the gain is greater than -6 dB. State control has a bandwidth of 23.2 Hz; good considering the open loop flutter frequency of 10.0 Hz. With ordinary Kalman estimators bandwidths are doubled or tripled.

Sensors 16 and 28 have no zeroes in the right half plane. Thus, the first (16, 57) and third (28) sensor complements meet asymptotic robustness requirements. Sensor 18 has a zero in the right half plane so robustness capabilities are expected to be more limited.

For each of the three sensor complements we used values for q of 0.000001, 0.00001, and 0.0001. Table 4 summarizes the results.

The RMS responses are generally monotone increasing with q . For the first case the increases are modest; even with $q = 0.0001$, the values of δ and $\dot{\delta}$ are acceptably small. For the non-minimum phase case (18), the increases in δ are very large and even with $q = 0.000001$ are in excess of objectives. For the minimum phase single sensor case (28) the increases with q are more modest.

Stability margins are also essentially monotone increasing with the robustness parameter q . Although negative phase margins are below objectives; we select $q = 0.000001$ as a compromise between RMS response and stability objectives.

Although not assured by theory it is no surprise that bandwidths are much smaller with the robust estimators.

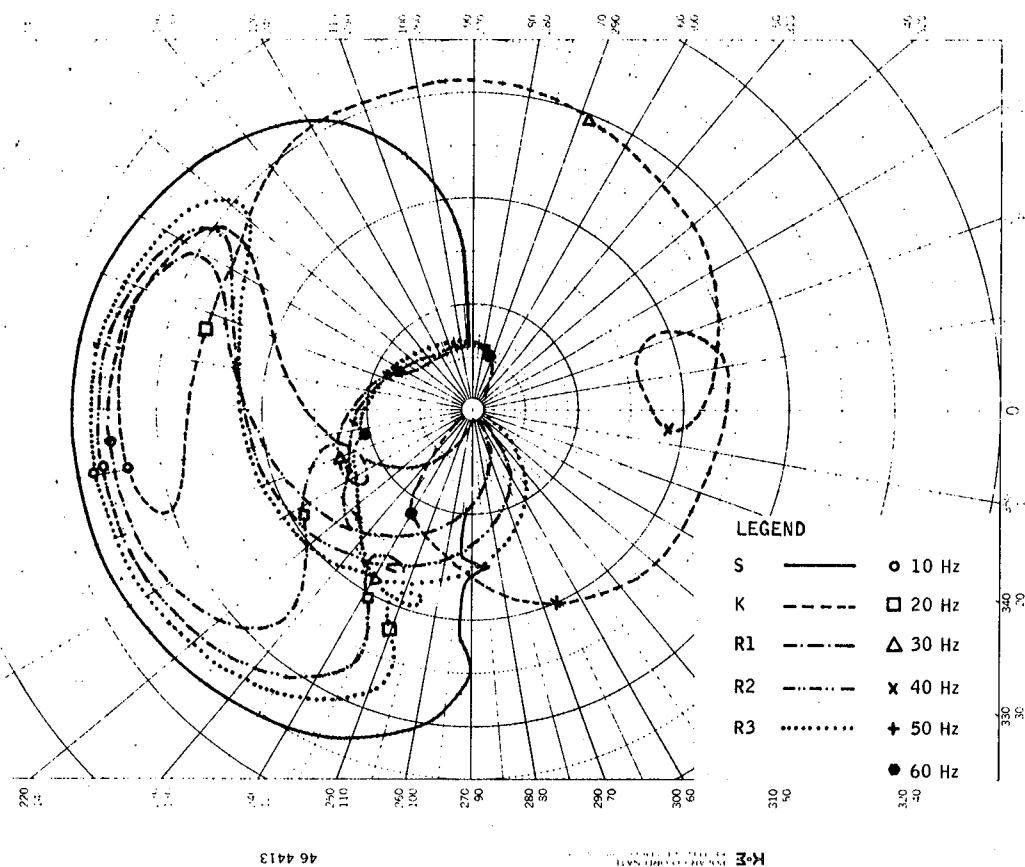


Figure 12. - Nyquist plot for node 18.

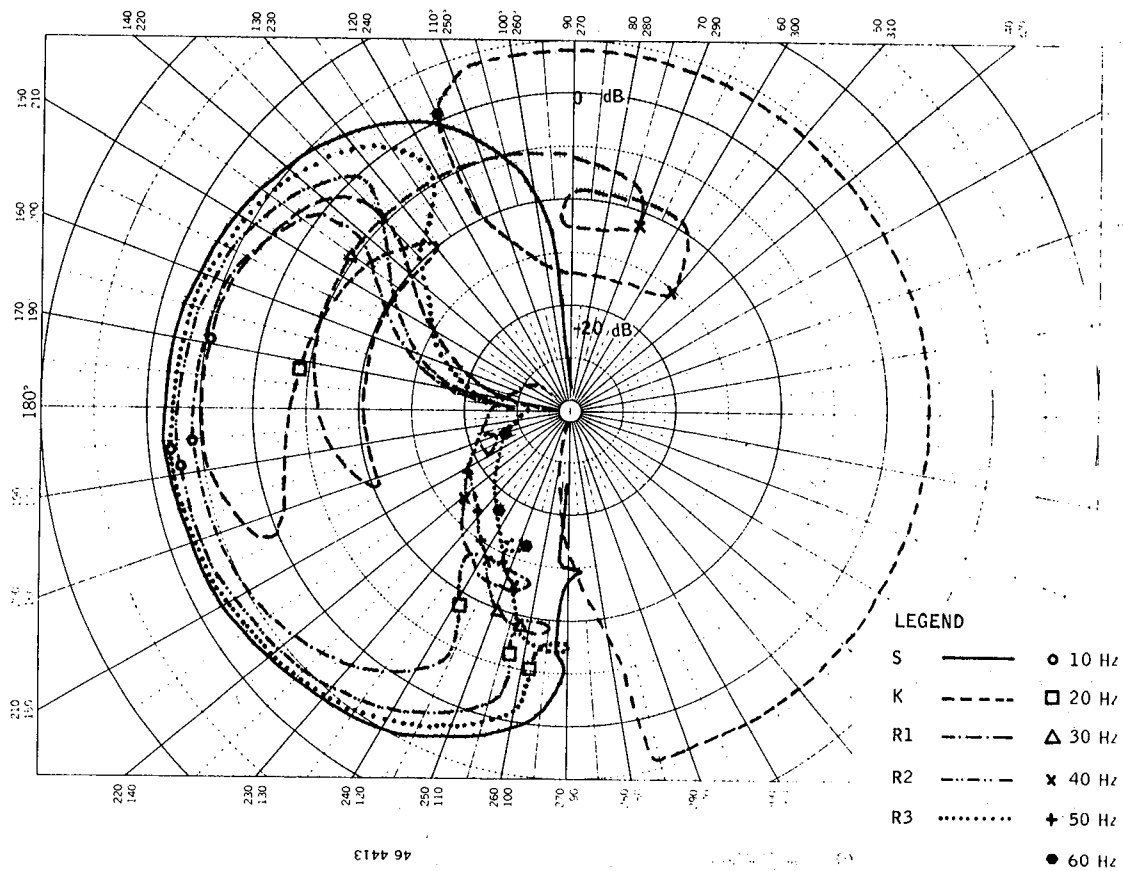


Figure 13. - Nyquist plot for node 28.

The Nyquist plot of Figure 11 for nodes 16, 57 demonstrates the effectiveness of the robust Kalman estimator synthesis procedure: monotonicity of margins and transition from Kalman estimator to full-state feedback as robustness increases. Low bandwidth is achieved at the lowest robustness level.

Figure 12 shows that with the non-minimum phase sensor, robustness is more difficult to achieve. With the minimum phase sensor (28) the results, Figure 13, are much like those of Figure 11.

Sensor Optimization

With the full-state feedback control law given, sensor positions are sought to achieve best system performance when implemented with a robust Kalman estimator. The single sensor and two sensor cases are considered.

Single sensor. -Previous considerations have amply demonstrated that the sensor should have minimum phase. We placed sensors at eight positions along the rear spar and two on the front spar and computed zeroes. They are presented in Table 5. Not surprising, considering ILAF (identical location of accelerometer and force), the three node positions (16, 19 and 22) on the rear spar and centered about the aileron are minimum phase. However, it was not anticipated that the range over which minimum phase is achieved would be so small.

The performance results of full-state feedback control are tabulated in row 1 of Table 6. Robust Kalman estimators with $q = 0.000001$ are synthesized with sensor at node points 16, 19 and 22, and the system performance evaluated are listed in rows 3-5 of Table 6. Node point 16 is better than node point 19 which is better than node point 22. This ordering correlates with the sensor zeroes (Table 5) meaning that more negative is better. The gain margins are good, but the phase margins need 15 to 20 deg increases in magnitude. The control surface deflection δ exceeds the objectives of 4.0

deg. Rates ($\dot{\delta}$) are below the objective of 250 deg/s. Increasing the robustness parameter q would increase the phase margins at the expense of RMS surface activity; and vice versa. So, we seek to improve performance by moving the sensor. We have exhausted the rear spar positions so we position them aft of the spar. The notation 19 (2T) indicates the point twice as far from the elastic axis as the node point 19 (Figure 14 shows the DAST ARW1 node points).

TABLE 5. -TWO MOST POSITIVE ZEROES*

Sensor node position		
2	+592.0	+592.0
4	+462.6	+462.6
7	+343.0	+343.0
10	+183.3	+183.3
13	+ 50.8	+ 50.8
16	- 9.1	- 9.1
19	- 7.5	- 7.5
22	- 6.1	- 6.1
6	732.8	+971.2
12	679.8	+679.8

*Neglecting both the two at zero
and the two wind zeroes at -4.5.

The last seven rows of Table 6 present the results. Moving aft and toward the tip improves performance. Although 4(3T) has better performance than 4(2T), we choose 4(2T) as our final result; 4(3T) is not used because we are concerned about accessibility.

Using the node point accelerometer 4(2T), gain margins are excellent, but we would like about 7.3 deg more phase margins. The surface rate and deflections meet the design specifications.

TABLE 6. SINGLE SENSOR ROBUST CONTROLLER PERFORMANCE

Control	Sensor node position	q	RMS per fps gust			J	Gain margin				Phase margin				Bandwidth
			δ	δ̇	u		dB	Hz	dB	Hz	Deg	Hz	Deg	Hz	
			Deg	Deg/sec											
State	---	0.0	2.579	189.4	2.630	0.5529×10 ⁶	-14.2	38.44	8.1	9.77	-65.1	6.72	95.1	14.21	86.3
Kalman	4(2T)	0.0	3.333	186.6	3.350	0.8565×10 ⁶	-3.7	23.76	7.3	10.44	-65.4	7.67	31.9	15.64	28.0
Robust	16	0.000001	4.047	218.7	4.584	0.1385×10 ⁷	-14.9	93.60	5.7	9.99	-43.3	7.93	48.6	12.80	16.2
Robust	19	0.000001	4.156	223.7	4.658	0.1484×10 ⁷	-15.1	94.33	5.5	9.99	-41.9	7.94	48.0	12.70	16.1
Robust	22	0.000001	4.201	225.1	4.693	0.1444×10 ⁷	-15.1	95.41	5.5	9.98	-41.7	7.94	48.0	12.68	16.1
Robust	19(2T)	0.000001	3.888	214.8	4.508	0.1361×10 ⁷	-14.6	102.56	6.3	10.03	-50.1	7.72	52.8	13.05	16.6
Robust	16(2T)	0.000001	3.788	207.8	4.391	0.1302×10 ⁷	-14.9	101.41	6.4	10.04	-51.7	7.70	52.7	13.13	16.9
Robust	13(2T)	0.000001	3.732	207.8	4.403	0.1310×10 ⁷	-14.5	101.41	6.4	10.04	-53.0	7.66	53.4	13.16	16.9
Robust	10(2T)	0.000001	3.683	207.0	4.371	0.1295×10 ⁷	-14.5	99.52	6.4	10.04	-52.2	7.67	53.1	13.19	16.9
Robust	7(2T)	0.000001	3.630	207.9	4.336	0.1283×10 ⁷	-14.5	98.01	6.5	10.06	-52.4	7.67	52.8	13.23	17.0
Robust	4(2T)	0.000001	3.595	209.7	4.314	0.1277×10 ⁷	-14.6	97.43	6.5	10.06	-52.7	7.66	52.7	13.24	17.0
Robust	4(3T)	0.000001	3.471	205.4	4.232	0.1253×10 ⁷	-14.3	105.52	7.0	10.07	-57.3	7.37	56.2	13.48	17.2

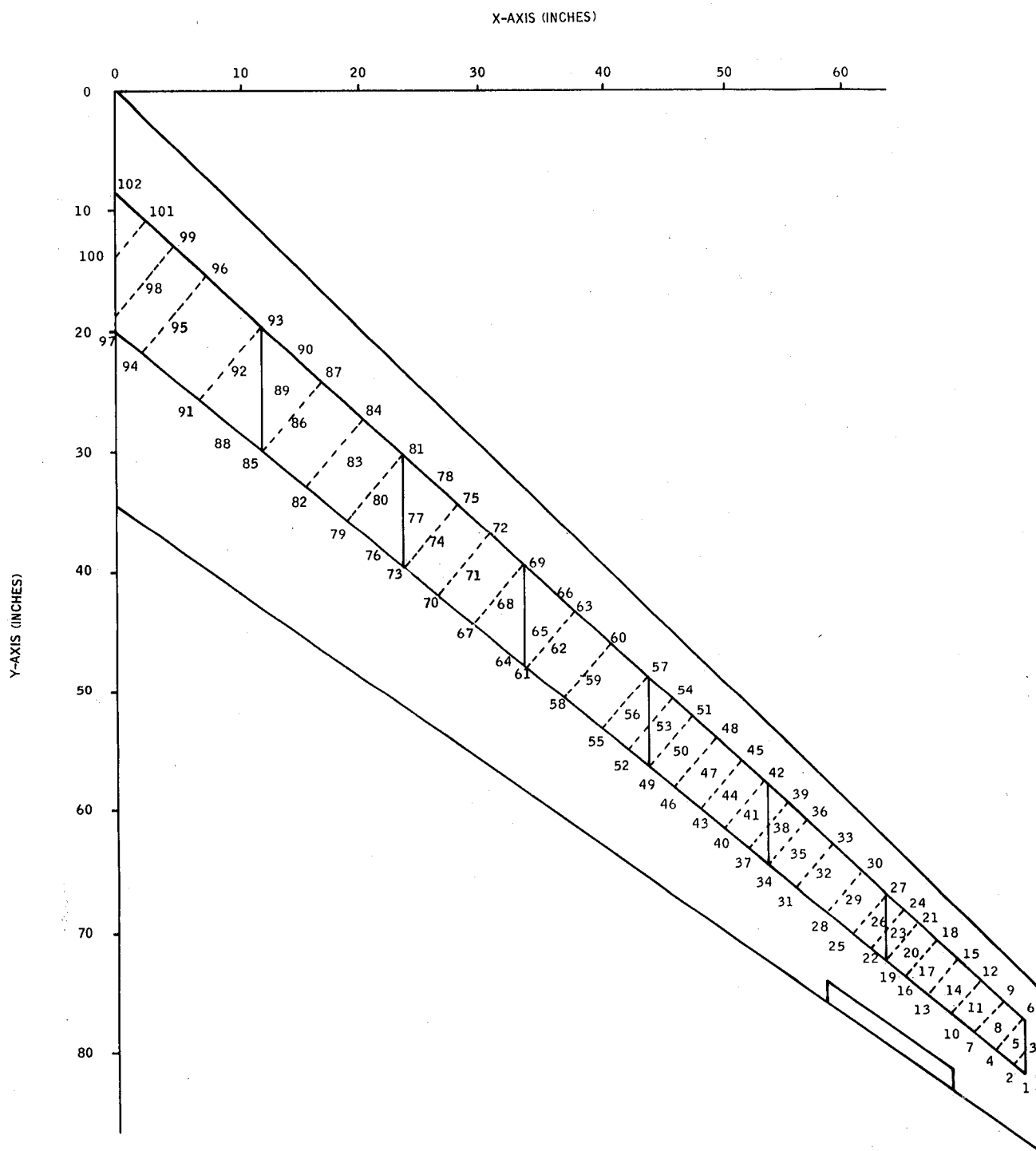


Figure 14. - DAST ARW1 node points.

A comparison (rows 2 and 11) of the results with the Kalman estimator and robust estimator for node points 4(2T) shows robustness cost 8 and 13 percent in deflection and rate. It improved the negative phase margin from the undesirable value of -3.7 to the desirable -14.6. Similarly, the positive phase margin increased from 31.9 to 52.7 deg and the bandwidth was reduced from 28.0 to 17.2 Hz. Using accelerometer positions 22 and 4(2T) as extremes, it is worthy of noting the benefits achieved by searching for better sensor positions. We improved δ by 14 percent, $\dot{\delta}$ by 7 percent and J by 12 percent. We also improved by 1.0 dB in positive gain margin, 9 deg in negative phase margin and 5 deg in positive phase margin.

Two sensors. -Here two methods are used to search for optimum sensor positions. The first is optimization of sensor location similar to that employed for the single sensor case. The second is a modification of the Stein-Harvey procedure (ref. 5).

For robust estimator design with two sensors and a single control, it is sufficient if some linear combination of the two sensors is minimum phase. Rather than attempt this calculation, we assume that if one of the accelerometers is near the aileron, then we can get minimum phase. As in the single sensor case, we start from a few promising positions and then perturb the positions to determine whether we are near a best position.

The first 20 rows of Table 7 present our results. The first row contains the full state-feedback results. Kalman and robust estimator data with sensors at nodes 2 and 6 are presented in rows 2 and 3. We consider these to be the best positions for sensors restricted to the front and rear spars. The robust aileron RMS value of 3.008 is considerably less than the objective of 4.0 and the RMS value for rate of 224.4 is slightly smaller than the objective of 250. The gain margins and bandwidth are good. We would like to increase the negative and positive phase margins by 20 and 8 deg, but believe the tradeoff with RMS responses to be undesirable.

TABLE 7. TWO SENSOR ROBUST CONTROLLER PERFORMANCE

Control	Sensor node positions	q	RMS per fps gust			J	Gain margin				Phase margin				Bandwidth
			δ	$\dot{\delta}$	u		dB	Hz	dB	Hz	Deg	Hz	Deg	Hz	Hz
			Deg	Deg/sec											
State		0.0	2.579	189.4	2.630	0.5529×10^6	-14.2	38.44	+8.1	9.77	-65.1	6.75	95.1	14.21	86.3
Kalman	2, 6	0.0	3.033	203.6	3.073	0.7501×10^6	-2.7	21.44	+5.6	10.42	-48.1	8.28	27.2	14.66	62.1
Robust	2, 6	0.000001	3.008	224.4	3.894	0.1051×10^7	-15.0	90.99	+5.7	9.92	-40.4	7.80	52.1	12.83	16.6
Robust	40, 42	0.000001	3.748	264.0	4.328	0.1325×10^7	-12.7	3.98	+5.1	9.85	-34.4	7.86	48.2	12.38	15.3
Robust	31, 33	0.000001	3.593	256.7	4.218	0.1238×10^7	-15.0	3.52	+5.3	9.85	-36.6	7.80	51.0	12.53	15.6
Robust	22, 27	0.000001	3.402	242.4	4.082	0.1151×10^7	-14.7	94.49	+5.6	9.87	-38.9	7.75	53.2	12.68	15.9
Robust	19, 21	0.000001	3.430	234.3	4.099	0.1150×10^7	-14.6	94.51	+5.6	9.88	-39.0	7.78	52.6	12.68	15.9
Robust	19, $\frac{21+18}{2}$	0.000001	3.446	231.2	4.111	0.1151×10^7	-14.6	94.54	+5.6	9.88	-39.0	7.78	52.5	12.68	15.9
Robust	19, 18	0.000001	3.463	228.4	4.123	0.1155×10^7	-14.6	94.62	+5.6	9.88	-39.0	7.78	52.4	12.68	15.9
Robust	$\frac{19+16}{2}, 18$	0.000001	3.413	227.8	4.088	0.1138×10^7	-14.6	94.22	+5.6	9.88	-39.3	7.78	52.6	12.72	16.1
Robust	16, 18	0.000001	3.368	227.0	4.057	0.1124×10^7	-14.6	93.95	+5.6	8.40	-39.6	7.78	52.8	12.73	16.2
Robust	16, 57	0.000001	3.232	237.5	3.988	0.1115×10^7	-14.6	93.68	+5.8	9.88	-40.7	7.73	54.3	12.83	16.4
Robust	16, 21	0.000001	3.345	232.3	4.041	0.1122×10^7	-14.6	93.85	+5.6	9.88	-39.5	7.77	53.0	12.73	16.1
Robust	10, 12	0.000001	3.278	220.6	3.988	0.1087×10^7	-14.8	91.93	+5.7	9.90	-40.0	7.80	52.3	12.78	16.4
Robust	4, 6	0.000001	3.200	222.9	3.926	0.1062×10^7	-14.9	91.72	+5.7	9.92	-40.4	7.80	52.3	12.81	16.4
Robust	4, 12	0.000001	3.177	223.4	3.484	0.1053×10^7	-15.2	89.72	+5.7	9.92	-40.0	7.81	51.7	12.81	16.6
Robust	16, 33	0.000001	3.263	241.4	3.985	0.1111×10^7	-14.6	93.73	+5.7	9.88	-39.7	7.73	53.7	12.76	16.2
Robust	10, 30	0.000001	3.216	232.6	3.938	0.1090×10^7	-14.7	90.59	+5.7	9.90	-39.7	7.77	52.7	12.78	16.4
Robust	19, 48	0.000001	3.289	243.5	3.989	0.1119×10^7	-14.6	94.14	+5.7	9.88	-39.9	7.72	54.2	12.76	16.2
Robust	4, 6(2T)	0.000001	2.984	214.2	3.788	0.9904×10^6	-14.7	105.09	+6.0	9.87	-44.3	7.61	57.7	12.88	16.4
Robust	16, 57*	0.000001	4.320	231.3	4.717	0.1447×10^7	-15.8	23.62	+5.0	9.96	-36.6	8.04	44.1	12.49	15.6
Robust	2, 12*	0.000001	3.706	240.1	4.388	0.1420×10^7	-16.4	87.87	+6.5	10.11	-51.2	7.59	49.7	13.32	17.5

* Blended to form a single sensor with gains given in Table 8.

$$\frac{m_1}{u} = \text{Transfer function of sensor 1}$$

$$\frac{m_2}{u} = \text{Transfer function of sensor 2}$$

The transfer function with numerical values is the unstable flutter mode that we are trying to match. In this sense, this is a minimum energy procedure (ref. 5).

To use the procedure, we select sensor positions, compute minimizing gains g_1 and g_2 and evaluate the least square cost J . The relative values of J for different sensor combinations are measures of relative merit. We then use the most likely candidates to synthesize a robust estimator to evaluate the final result.

Table 8 shows results for the least squares part of the procedure. Sensor node positions are presented in column 1. Nodes 16 and 57 and their perturbations in the next three combinations were selected on the basis of control-observe-ability (Section IV). The last six combinations are the best candidates based on achieving minimal controller cost. The costs (column 4) are not markedly different. The first four have lower costs with the combination at 16, 57 being minimal. Node combination 2, 12 has minimal magnitude for gains g_1 and g_2 ; this might be significant when we evaluate system performance using realistic sensor noise.

We selected 16, 57 and 2, 12 for further consideration. Robust estimators were synthesized and the systems evaluated. Rows 21 and 22 of Table 7 present the results. They are worse than most others. The node 2, 12 combination is better than that for the node 16, 57 combination. In this case the magnitude of the sensor noise is an important consideration for sensor placement.

TABLE 8. -SENSOR FREQUENCY RESPONSE MATCHING

Sensor node position	g_1	g_2	Σe^2
16, 57	-0.4333	-0.2516	0.3139E + 09
13, 57	-0.3948	-0.3568	0.3239E + 09
13, 54	-0.3877	-0.3429	0.3227E + 09
10, 54	-0.3483	-0.4225	0.3327E + 09
2, 6	-0.4988	+0.3492	0.3891E + 09
2, 9	-0.4424	+0.2977	0.4047E + 09
2, 12	-0.3569	+0.1950	0.4183E + 09
4, 12	-0.4129	+0.2428	0.4027E + 09
4, 6	-0.5448	+0.3652	0.3723E + 09
4, 6 (2T)	-0.4213	+0.2412	0.3719E + 09

SECTION VI

PRACTICAL FLUTTER CONTROLLERS

The robust Kalman estimator together with the optimal state feedback gains constitute the optimal controller that can be implemented. However, the cost of implementation can be significantly reduced by developing lower order approximations to the optimal controller. The low-order approximations that satisfy the performance requirements are called practical controllers. Two methods of developing practical controllers from the optimal controller are residualization and frequency response matching (ref. 4 and 5). These methods are used to develop practical flutter controllers for the DAST ARW1 wing. Also a practical flutter controller is evaluated at various mach numbers and dynamic pressures to check its operation throughout the flight envelope.

Practicalization (Simplification) Procedure

In simplification, we are attempting to approximate the high order optimal controllers with a much lower order approximation that

- Achieves closed loop asymptotic stability
- Maintains ample gain and phase margins
- Maintains low band width
- Does not markedly increase RMS responses

We tacitly assume that if we approximate the low-frequency characteristics with an approximation that ultimately has 40 dB rolloff per decade (to satisfy high frequency actuator limitations) then we will meet the objectives.

The optimal controller is given by the equations (41) and (42).

$$\dot{\hat{x}} = (A + B_1K + LC)\hat{x} - Lm \quad (41)$$

$$u = K\hat{x} \quad (42)$$

where

\hat{x} is the state of the robust Kalman estimator

K is the optimal state feedback gains

L is the robust Kalman estimator gains

The low-order approximations are determined as equations (43) and (44).

$$\dot{\hat{x}}_1 = \bar{A}\hat{x}_1 + \bar{B}m \quad (43)$$

$$u = \bar{C}\hat{x}_1 + \bar{D}m \quad (44)$$

where

\hat{x}_1 is the state of the low order system.

Two methods of obtaining \bar{A} , \bar{B} , \bar{C} and \bar{D} matrices are described in the following.

Residualization. -Here the optimal control system is split into two parts as shown by equation (45) and (46).

$$\begin{aligned} \begin{bmatrix} \dot{\hat{x}}_1 \\ \dot{\hat{x}}_2 \end{bmatrix} &= \begin{bmatrix} A_{11} & A_{12} \\ A_{21} & A_{22} \end{bmatrix} \begin{bmatrix} \hat{x}_1 \\ \hat{x}_2 \end{bmatrix} + \begin{bmatrix} [B_1K]_1 & [B_1K]_2 \end{bmatrix} \begin{bmatrix} \hat{x}_1 \\ \hat{x}_2 \end{bmatrix} \\ &+ \begin{bmatrix} (LC)_1 & (LC)_2 \end{bmatrix} \begin{bmatrix} \hat{x}_1 \\ \hat{x}_2 \end{bmatrix} - \begin{bmatrix} L_1 \\ L_2 \end{bmatrix} m \end{aligned} \quad (45)$$

$$u = \begin{bmatrix} K_1 & K_2 \end{bmatrix} \begin{bmatrix} \hat{x}_1 \\ \hat{x}_2 \end{bmatrix} \quad (46)$$

In the first part (low frequency portion) the dynamics is retained. In the second part (high frequency portion) only the static terms are retained. The static terms are obtained by setting $\dot{\hat{x}}_2 = 0$ and are given by

$$\hat{x}_2 = -[A_{22} + (B_1 K)_2 + (LC)_2]^{-1} [A_{21} x_1 - L_2 m] \quad (47)$$

Using equation (47) the residualized system is given by

$$\begin{aligned} \dot{\hat{x}}_1 = & \left\{ A_{11} + (B_1 K)_1 + (LC)_1 - A_{12} [A_{22} + (B_1 K)_2 + (LC)_2]^{-1} A_{21} \right\} \hat{x}_1 \\ & - \left\{ L_1 - A_{12} [A_{22} + (B_1 K)_2 + (LC)_2]^{-1} L_2 \right\} m \end{aligned} \quad (48)$$

$$\begin{aligned} u = & \left\{ K_1 - K_2 [A_{22} + (B_1 K)_2 + (LC)_2]^{-1} A_{21} \right\} \hat{x}_1 \\ & + K_2 [A_{22} + (B_1 K)_2 + (LC)_2]^{-1} L_2 m \end{aligned} \quad (49)$$

For the practical controllers the rolloff requirement is 40 dB/decade. In the examples we worked, the direct transfer matrix is small. So we often discarded this term and provided a single rolloff filter at 300. rad/sec to meet rolloff requirements. Alternatively, we can retain the direct transfer and append another filter at 3000. rad/sec.

Frequency response matching.—This procedure (as the name implies) involves obtaining a low-order transfer function approximation to the optimal controller over a frequency band of interest.

The transfer function between measurement m and control u (from equations 41 and 42) is given by

$$u = K(sI - A - B_1 K - LC)^{-1}(-L)m \quad (50)$$

$$\Delta T(s)m$$

For the single control variable case with two measurements

$$u = \begin{bmatrix} T_1(s) & T_2(s) \end{bmatrix} \begin{bmatrix} m_1 \\ m_2 \end{bmatrix} \quad (51)$$

With one measurement, T_2 and m_2 are zero. In frequency response matching we approximate each $T_i(s)$ with a low-order rational transfer function $T_{ai}(s)$. The numerator and denominator orders are selected and we can choose to restrict the $T_{ai}(s)$ to be stable and/or minimum phase. Then, the coefficients of $T_{ai}(s)$ are calculated to minimize

$$J = \sum_k \omega_k W(\omega_k) |T_i(\omega_k) - T_{ai}(\omega_k)|^2 \quad (52)$$

where

ω_k is a set of points in the frequency band of interest

$W(\omega_k)$ is a weighting function.

Practicalization Results

Here, the optimal flutter controller, obtained with a second-order Dryden wind model, is simplified to obtain three practical flutter controllers. Two of them use a single sensor aft of wing node point 4. The first approximates the optimal flutter controller by residualization and the second approximates it by frequency response matching; the approximate filters are of fourth and fifth orders respectively. The third employs two sensors at node points 2 and 6 and is obtained from a seventh-order residualization of the optimal controller. All controllers meet the RMS requirements. Stability margins are reasonably good.

Single sensor practicalization results. -Table 9 presents the performance results. Rows 1, 2, and 3 show the state, Kalman and robust results discussed previously. Rows 4 and 5 summarize results with our best residualized controller. It is obtained by retaining the first two flexure nodes in the estimator, by deleting the small direct transfer term (No D), and by adding a first-order lag with a 1/300 sec time constant to meet rolloff requirements. In row 4 the sensor measurement noise is set to zero to permit showing its effect on system performance. A comparison of rows 3 and 5 show that residualization has reduced RMS activity. The RMS deflection of 3.41 deg and rate of 184.3 deg/sec are well below the objective of 4 deg and 250 deg/sec respectively. The adverse effect of residualization is in the reductions in stability margins. The gain margins of -5.0 and +5.5 are below the objective of ± 6.0 dB. We also suffered a 13 deg of positive phase margin to reduce its value to about 40 deg. The increase in bandwidth from 17.0 to 25.6 Hz is acceptable.

Similar results were obtained with frequency response matching using a second over third approximation. The RMS values are essentially the same, gain margins are good, but we lost another 4 deg in positive phase margin.

Figure 15 presents the Bode plots for the state, Kalman, robust, residualized and transfer function approximation cases. The figure shows that achieving the desired RMS response at the full-state feedback design level force excessive bandwidth on the system. Both practical controllers achieve good rolloff after 23.9 Hz.

Two sensors practicalization results. -Table 10 presents the performance summary. Rows 1, 2, and 3 are for state control and control with Kalman and robust estimators. Rows 4 and 5 are for our best controller obtained by retaining the first two flexure modes and the gust filter (G) of the estimator during residualization; the small direct transfer term was dropped (No. D) and the rolloff filter added. The effect of residualization was to yield a small but acceptable increase in RMS control surface deflection and a decrease in

TABLE 9. SINGLE SENSOR PRACTICAL CONTROLLER PERFORMANCE

Control	Sensor node position	RMS			Gain margin				Phase margin				Bandwidth	Retained Components	Added Filters
		δ	$\dot{\delta}$	u											
		Deg	Deg/sec	Deg	dB	Hz	dB	Hz	Deg	Hz	Deg	Hz	Hz		
State*	---	2.58	189.4	2.630	-14.2	38.4	8.1	9.8	-65.1	6.7	95.1	14.2	86.3	All	
Kalman	4(2T)	3.33	186.6	3.350	-3.7	23.8	7.3	10.4	-65.4	7.7	31.9	15.6	28.0	All	
Robust	4(2T)	3.59	209.7	4.314	-14.6	97.4	6.5	10.1	-52.7	7.7	52.7	13.2	17.0	All	
RESID*	4(2T)	3.16	180.3	3.172	-5.0	23.7	5.5	10.2	-65.5	8.1	39.6	16.1	25.6	1,2, No D	$\frac{300}{S+300}$
RESID	4(2T)	3.41	184.3	3.346	-5.0	23.7	5.5	10.2	-65.5	8.1	39.6	16.1	25.6	1,2, No D	$\frac{300}{S+300}$
TRNFN*	4(2T)	3.23	184.3	3.246	-8.3	30.4	6.5	10.4	-60.7	7.7	35.4	12.9	27.1	2/3	$\frac{300}{S+300}$
TRNFN	4(2T)	3.42	189.3	3.434	-8.3	30.4	6.5	10.4	-60.7	7.7	35.4	12.9	27.1	2/3	$\frac{300}{S+300}$

*Without sensor measurement noise

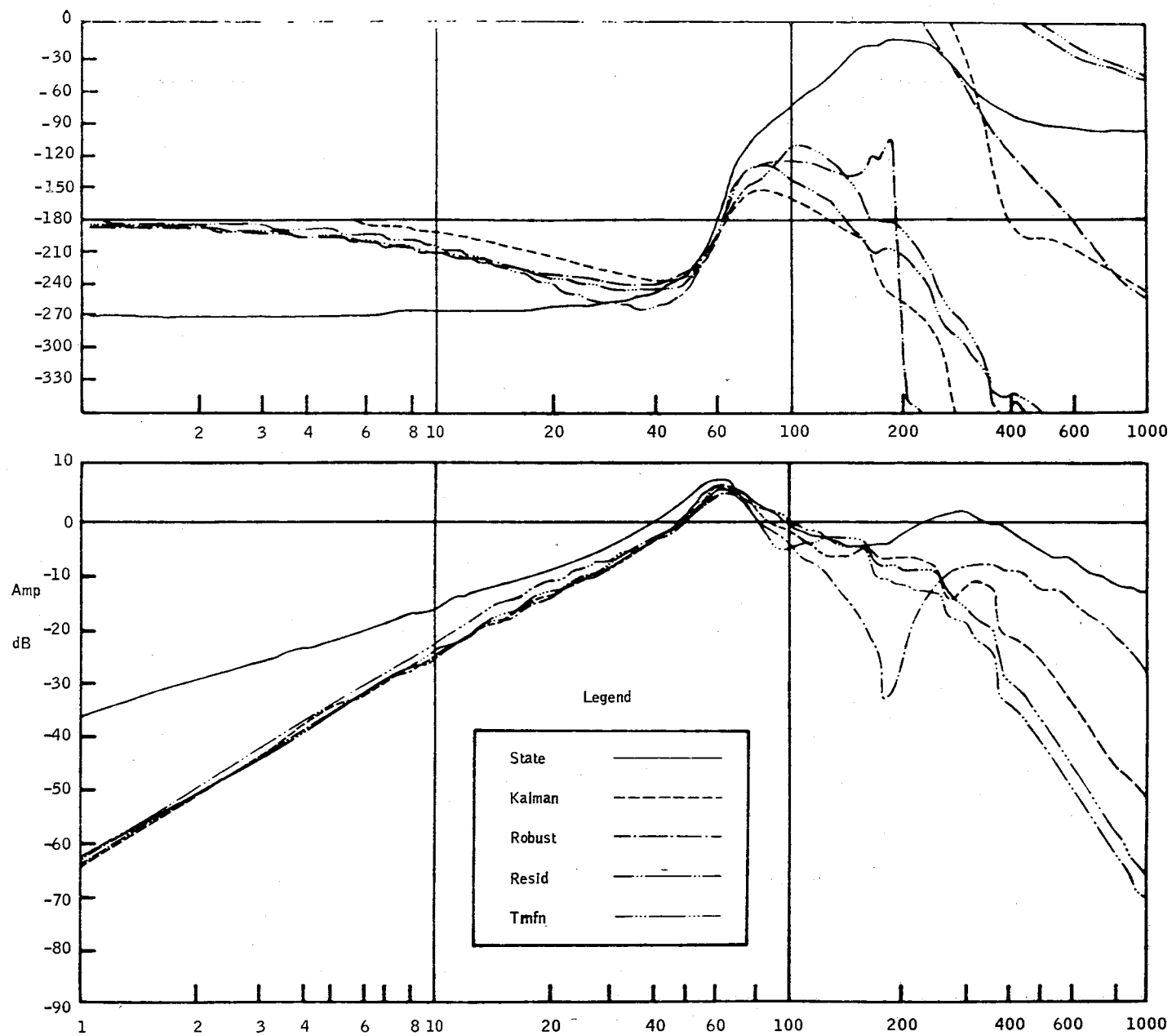


Figure 15. - Bode plots for single sensor 4(2T)

TABLE 10. TWO SENSOR PRACTICAL CONTROLLER PERFORMANCE

Control	Sensor node positions	RMS			Gain margin				Phase margin				Bandwidth	Retained Components	Added Filters
		δ	$\dot{\delta}$	u											
		Deg	Deg/sec	Deg	dB	Hz	dB	Hz	Deg	Hz	Deg	Hz	Hz		
State*	---	2.58	189.4	2.63	-14.2	38.4	8.1	9.8	-65.1	6.7	95.1	14.2	86.3	All	
Kalman	2,6	3.03	203.6	3.07	-2.7	21.4	5.6	10.4	-48.1	8.3	27.2	14.7	62.1	All	
Robust	2,6	3.01	224.4	3.89	-15.0	91.0	5.7	9.9	-40.4	7.8	52.1	12.8	16.6	All	
RESID*	2,6	3.04	197.6	3.05	-5.7	23.3	3.8	10.1	-52.0	8.2	61.1	12.8	23.9	1,2, G, No D	$\frac{300}{S+300}$
RESID	2,6	3.27	215.3	3.28	-5.7	23.3	3.8	10.1	-52.0	8.2	61.1	12.8	23.9	1,2, G, No D	$\frac{300}{S+300}$

*Without sensor measurement noise

rate. Phase margins are improved and are acceptable. Most serious is the loss in positive gain margin.

Figure 16 compares the frequency responses of state, Kalman robust and residualized controllers. We see that the Kalman control attempts to maintain the high bandwidth of the state control. The bandwidth of the robust is much smaller than that for the Kalman. The residualized practical controller is quite similar to the robust.

Practical flutter controllers. - The three final design controllers are presented in Table 11. The two single sensor controllers look good. They are stable and minimum phase. Poles and zeros are neither excessively large nor small. The two sensor controller (obtained by residualization) is non-minimum phase. The transfer from sensor 6 has a zero in the right half plan. Otherwise, the controller is satisfactory.

Performance Analysis of the Final Flutter Controller

The residualized practical controller with the sensor (accelerometer) located at a point on the wing twice as far from the elastic axis as node point 4 is chosen to be the final practical controller for further evaluation. The sensor location is marked on Figure 14 which shows the DAST ARW1 node points. Its (x,y) coordinates are 2.022 m and 1.780 m. The flutter controller transfer function is given by the equation

$$\frac{\delta_{ac}}{\ddot{h}} = \frac{1.1961}{(s + 300)} \frac{(s^2 + 116.7276 s + 7819.8649)}{(s^2 + 73.6256 s + 2829.1761)} \frac{(s + 22.91)}{s^2 + 28.0845 s + 362.1409} \quad (53)$$

where δ_{ac} is the input to the actuator and h is the vertical displacement of the wing at the accelerometer location. The flutter controller was designed

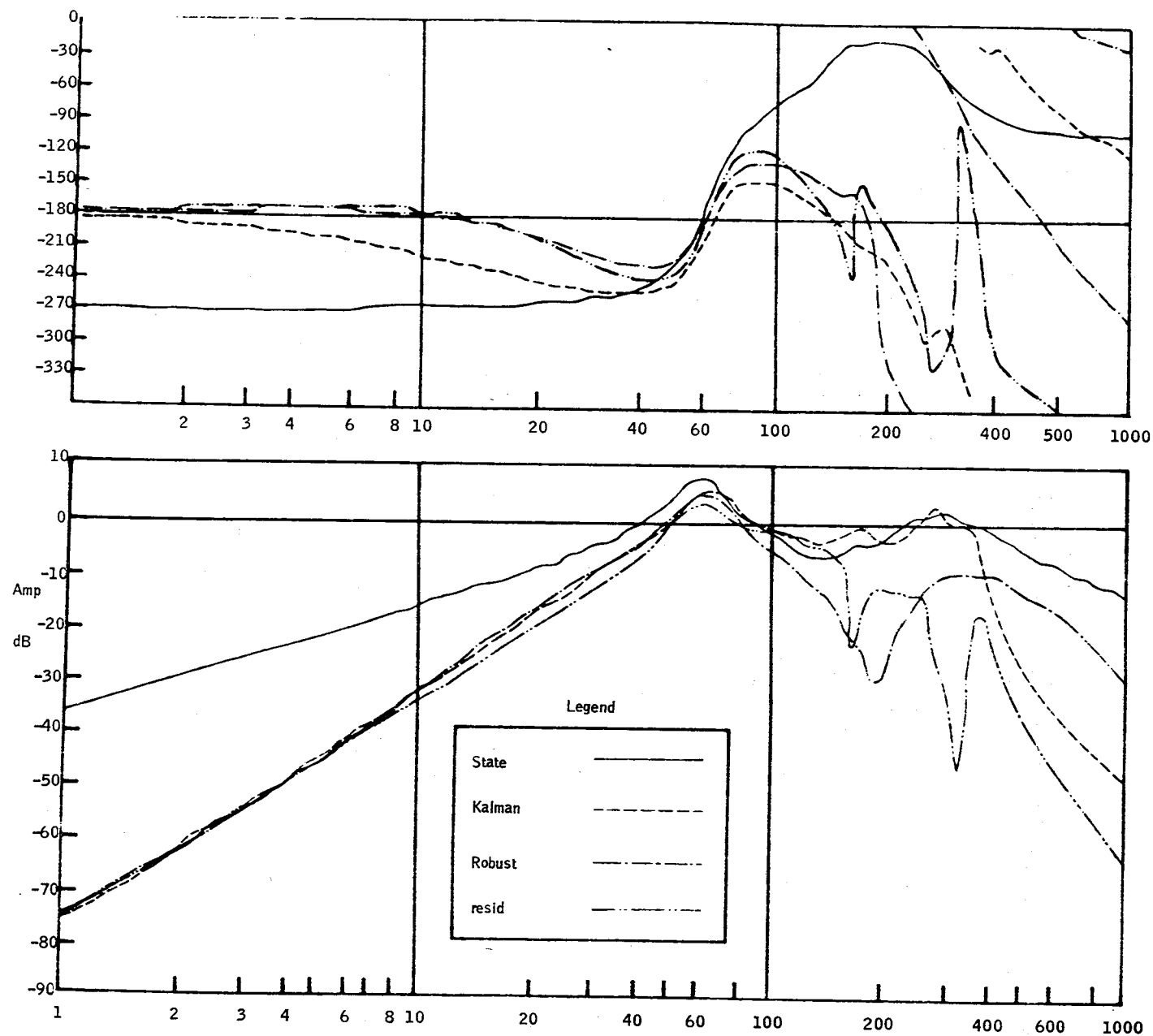


Figure 16. - Bode plots for two sensors 2 and 6.

TABLE 11. - PRACTICAL CONTROLLER TRANSFER FUNCTIONS

Method	Sensor	Transfer functions
RESID	4(2T)	$(0.003987) \frac{(300) (S^2 + 2. * 0.6600 * 88.43 S + 88.43^2) (S + 22.91)}{(S+300) (S^2 + 2. * 0.6921 * 53.19 * S + 53.19^2) (S^2 + 2. * 0.7379 * 19.03 * S + 19.03^2)}$
TRNFN	4(2T)	$(0.006855) \frac{(300) (S^2 + 2. * 0.1496 * 92.57 * S + 92.57^2)}{(S + 300) (S^2 + 2. * 0.4247 * 70.04 * S + 70.04^2) (S + 17.65)}$
RESID	2	$(0.009367) \frac{(300) (S^2 + 2. * 0.6258 * 18.57 * S + 18.57^2) (S^2 + 2. * 0.9991 * 4.477 * S + 4.477^2) (S + 158.)}{(S + 300) (S^2 + 2. * 0.6818 * 26.73 * S + 26.73^2) (S^2 + 2. * 0.9938 * 7.498 * S + 7.498^2) (S + 154.9) (S + 3.973)}$
	6	$(-0.010467) \frac{(300) (S^2 + 2. * 0.9989 * 4.488 * S + 4.488^2) (S - 20.64) (S + 97.06) (S + 20.01)}{(S + 300) (S^2 + 2. * 0.6818 * 26.73 * S + 26.73^2) (S^2 + 2. * 0.9938 * 7.498 * S + 7.498^2) (S + 154.9) (S + 3.973)}$

by considering the DAST half-wing model with one aerodynamic lag term ($L=1$) and 5 modes. In the following analysis the DAST half-wing will be represented by different models. (by changing the number of lag terms and modes considered) and the flutter controller will be evaluated. In addition, the performance of the flutter controller as the mach number and dynamic pressure change will be studied.

Performance with different models. -Table 12 shows the evaluation with four different models for DAST half wing. The first model is used during the design. We notice that the RMS values go up as more number of modes and aerodynamic lag terms are included. The gain and phase margins do not change considerably. The bandwidth is about constant except in the case of fourth model. The fourth model with number of lag terms equal to four and number of modes equal to eight is considered to be the most accurate representation of the DAST half wing. The fifth model is identical to the fourth except that there is no sensor noise. So the gain margin, phase margin, and bandwidth data are identical to that of the fourth model. The difference in the RMS values for the control surface between the fourth and fifth model is due only to the sensor noise.

Performance at different mach numbers and dynamic pressures. -Here the model used contains four aerodynamic lag terms and five modes. The results are presented in Table 13. We notice that the RMS values at any Mach number increases as the dynamic pressure is increased. Also, the bandwidth of the system increases as the dynamic pressure is increased. In terms of stability, the worst gain margin is 2.91 dB and the worst phase margin is -14.81° (note that both of these are at dynamic pressure of 9.58 k Pa). If we restrict the dynamic pressure to be less than 7.66 k Pa , the worst gain margin is 3.03 dB and the worst phase margin is 25.6° . Table 14 presents the fluter dynamic pressure and the flutter frequency for the three Mach numbers. At Mach number 0.9 the dynamic pressure at which the DAST half wing flutters is more than doubled with the flutter controller.

TABLE 12. PERFORMANCE VARIATION WITH DIFFERENT APPROXIMATIONS
TO THE DAST HALF WING (MACH NO. = 0.9 q = 7.66 k PAS)

No.	Model used for DAST half wing	Control surface deflection (RMS) (Deg)	Control surface velocity (RMS) (Deg/sec)	Gain margin				Phase margin				Bandwidth
				dB	Hz	dB	Hz	Deg	Hz	Deg	Hz	Hz
1	L = 1 ; 5 modes	3.41	184.33	-5.0	23.7	5.5	10.20	-65.5	8.10	39.6	16.1	25.6
2	L = 1 ; 8 modes	3.41	183.25	-4.9	23.7	5.6	10.17	-63.1	8.12	39.1	16.1	25.6
3	L = 4 ; 5 modes	3.85	207.67	-5.5	23.8	5.21	9.84	-55.36	8.11	36.7	16.2	25.6
4	L = 4 ; 8 modes	3.87	207.92	-5.4	23.8	5.23	9.81	-52.6	8.14	36.3	16.3	27.1
5	L = 4 ; 8 modes (No sensor noise)	3.65	204.17	-5.4	23.8	5.23	9.81	-52.6	8.14	36.3	16.3	27.1

TABLE 13. - PERFORMANCE VARIATION WITH MACH NUMBER AND DYNAMIC PRESSURE FOR THE DAST HALF WING

Mach number	Dynamic pressure q (k Pa)	Control surface deflection (RMS) (Deg)	Control surface velocity (RMS) (deg/sec)	Gain margin				Phase margin				Bandwidth Hz
				dB	Hz	dB	Hz	Deg	Hz	Deg	Hz	
0.7	3.83	1.79	84.63	-13.47	23.83	-	-	-104.5	4.19	27.27	9.36	17.7
	5.75	2.88	173.38	-10.07	23.83	-	-	-112.76	4.76	27.12	10.57	18.5
	7.66	4.44	284.88	-7.68	23.81	3.03	10.92	-103.5	8.67	34.32	14.30	20.2
	9.58	4.80	279.54	-5.83	23.77	2.91	10.84	-23.84	9.02	22.39	14.98	24.5
0.8	3.83	1.88	90.18	-12.54	23.81	-	-	-104.62	4.25	25.60	9.34	18.3
	5.75	3.02	177.96	-9.15	23.84	19.19	8.88	-113.89	5.02	29.54	10.38	19.4
	7.66	4.05	240.81	-6.78	23.84	3.95	10.42	-73.80	8.64	37.08	15.01	21.6
	9.58	4.95	257.55	-4.95	23.83	4.16	10.29	-22.38	8.09	25.48	15.93	25.6
0.9	3.83	2.03	97.93	-11.17	23.62	-	-	-105.38	4.37	24.32	9.27	18.8
	5.75	3.09	173.15	-7.85	23.77	13.41	9.03	-114.27	5.48	37.88	10.15	20.7
	7.66	3.85	207.70	-5.48	23.82	5.21	9.84	-55.36	8.11	36.70	16.23	25.6
	9.58	6.07	274.91	-3.65	23.84	5.68	9.69	-14.81	7.06	25.84	17.44	27.1

Figures 17 and 18 present the root locus at Mach 0.9 of the eight modes as the dynamic pressure is varied (here the model contains four aerodynamic lag terms and eight modes), with and without the flutter controller.

TABLE 14. - FLUTTER DYNAMIC PRESSURE AND FLUTTER FREQUENCY VARIATION WITH MACH NUMBER FOR THE DAST HALF WING

Mach number	Without flutter suppression control		With flutter suppression control	
	\bar{q}_f (k Pa)	f_f (Hz)	\bar{q}_f (k Pa)	f_f (Hz)
0.7	6.32	9.266	11.72	6.871
0.8	5.75	8.650	11.08	6.584
0.9	4.96	8.029	10.39	6.272

The performance analysis indicates that the flutter controller more than achieves the required 44 percent increase in flutter dynamic pressure. At the design point of Mach number 0.9 and dynamic pressure of 7.66 k Pa , the RMS activity of the control surface deflection and rate are within the design objectives. Also the gain margin, phase margin and bandwidth are satisfactory. However, over the range of mach numbers and dynamic pressures considered, the gain margins and phase margins are not entirely satisfactory (with constant gain flutter controller). This indicates the need for gain scheduling of the flutter controller over the range of operation.

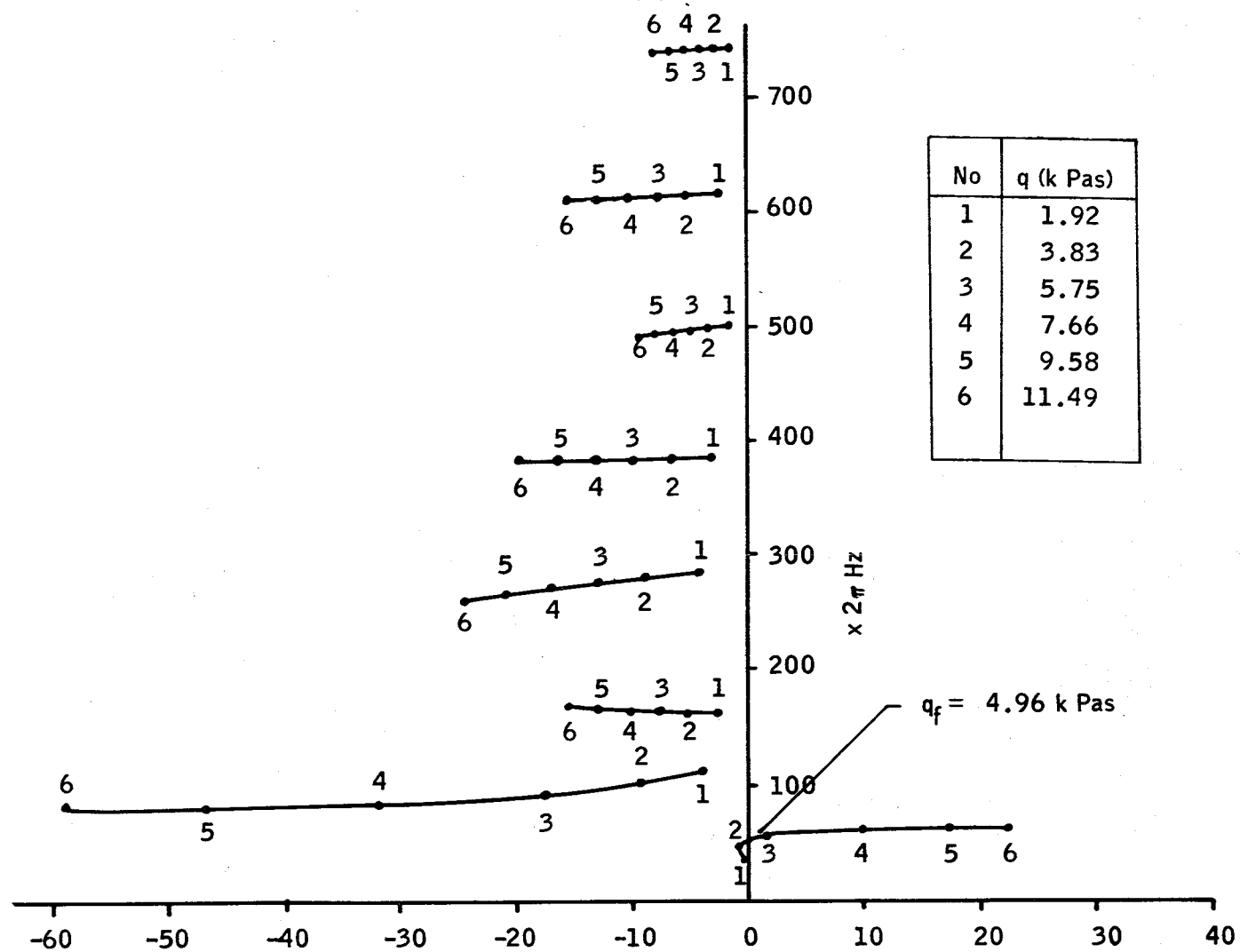


Figure 17.- Root locus at $M = 0.9$ (open loop).

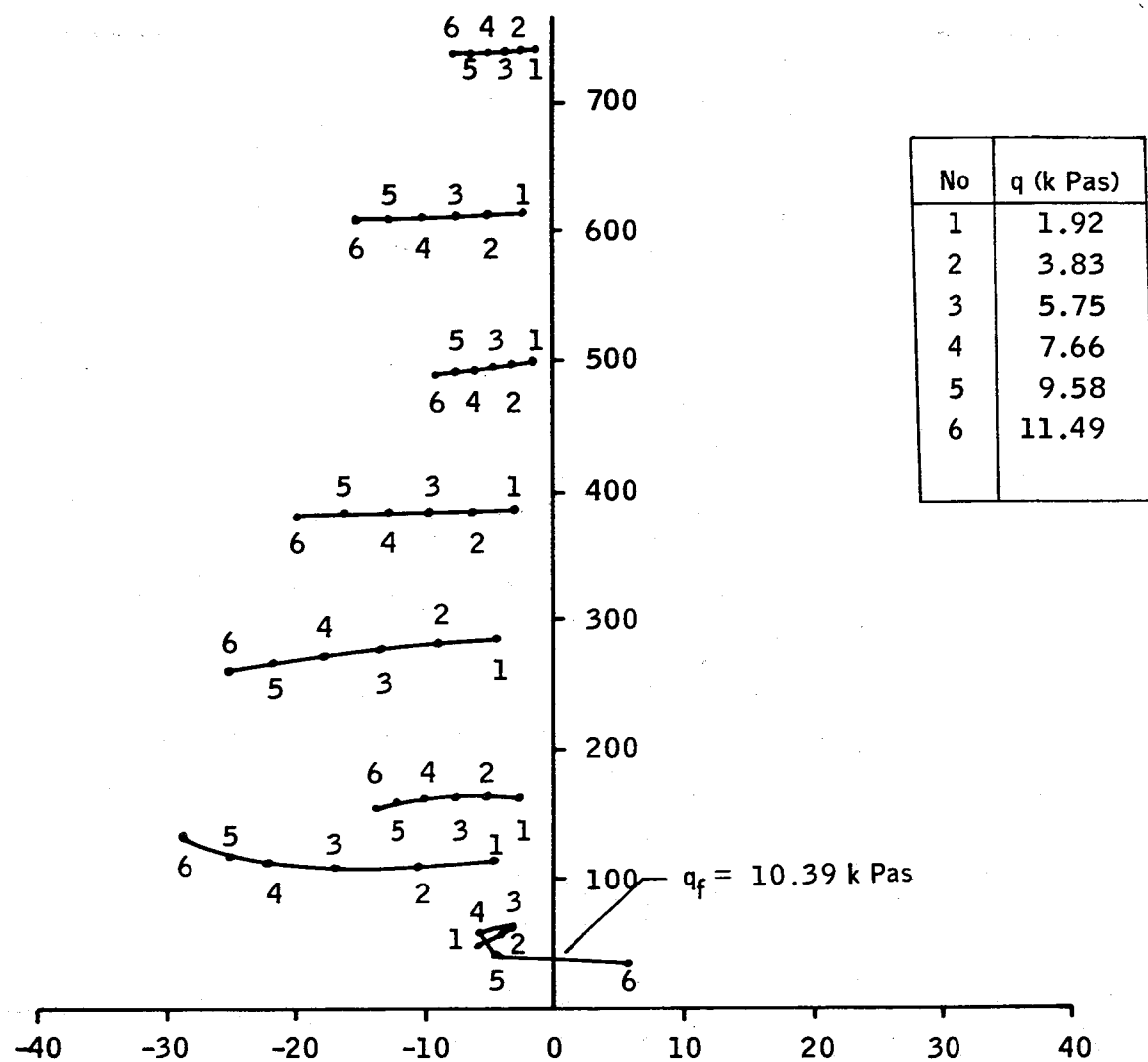


Figure 18.- Root locus at $M = 0.9$ (flutter suppression control).

SECTION VII

CONCLUSIONS AND RECOMMENDATIONS

The objectives of this study were four fold:

- 1 Develop an active flutter control methodology
- 2 Design a flutter controller for DAST ARW1 wing to increase the flutter speed by 20 percent
- 3 Investigate methods for surface/sensor placement, and
- 4 Update NASA owned KONPACT software with respect to modeling procedures and design methods developed during the course of this study.

These objectives were primarily met. The active flutter control methodology, the summary of design results for the DAST ARW1 wing and the results of surface/sensor placement are presented in this volume. The detailed technical results, documented as customer engineering letters during this study, have been collected as appendices and presented in Volume II. The modifications to KONPACT software are documented in Volume III.

In the following, the results and recommendations for future work in the area of active control technology are presented.

Significant Results

- An active control methodology was successfully applied to design a flutter suppression control for DAST ARW1 wing to increase the flutter speed by 20 percent.

- Effective procedures were investigated and applied to the surface/sensor placement to improve the performances significantly.
- An automated procedure was implemented to model the unsteady aerodynamics of the DAST ARW1 wing and effectively interface KONPACT with the NASTRAN software.

Recommendations for Future Work

- Develop and apply an integrated active control methodology to meet the multiple design criteria which include flutter suppression, rigid body control specifications, and other demands (such as maneuver load control and gust load alleviation).
- Implement algorithms for application of symmetric singular value analysis (ref. 19) to study the robustness of multiloop systems.
- Implement algorithms to develop low order transfer functions (having the same denominator) to match the frequency response of multi input multi output system. This will simplify the task of obtaining minimal order practical controllers.
- Develop efficient algorithms to solve the constrained optimal control problems to enforce conventional design criteria into optimal active control synthesis techniques.
- Develop design procedures using residualized Riccati equations via singular perturbation and boundary layer techniques (ref. 20, 21) to reduce design cost for high order systems.
- Add optimal digital control analysis and design algorithms to KONPACT software.

- The existing optimal control routines (particularly FFOC: Fixed Form Optimal Control) should be revised for higher computational efficiency.

Conclusions

- Active control methodology, based on linear quadratic Gaussian theory, is viable for design of flutter suppression systems for flexible vehicles.
- Optimization of surface/sensor placement offers significant performance improvement.
- Use of a lower order approximate model for the flexible wing during the flutter control design and verifying the performance of the final controller with a higher order more exact model of the flexible wing reduces the computer cost of design significantly.
- Present design objective, for the DAST ARW1 wing, relative to RMS and stability requirements are too demanding. More aileron effectiveness (by increasing aileron span) would provide the flutter control designer freedom necessary to allow design of a practical flutter controller that meets the RMS and stability requirements more easily.

REFERENCES

1. A. F. Konar and J. K. Mahesh, "Computer Programs for Active Control Technology, "Volume III, User's Manual, AFFDL-TR-75-146, Vol III, August 1976.
2. Jones, R. T., "The Unsteady Lift of a Wing of Finite Aspect Ratio," NACA Rept. 681, 1940.
3. Safonov, M. G., and Athans, "Gain and Phase Margin of Multiloop LQG Regulators," IEEE Trans. Auto Control, " April 1977.
4. A. F. Konar, et al, "Active Control Synthesis for Flexible Vehicles" Vol I, AFFDL-TR-75-146, June 1976.
5. Stein, G. and Harvey, C. A., "Adaptive Control of Wing/Store Flutter," AFFDL-TR-79-3081, April 1979.
6. Severt, F. D. "Development of Active Flutter Suppression Wind Tunnel Testing Technology," AFFDL-TR-74-126, 1975.
7. Abel Irving et al, "Synthesis of Active Controls for Flutter Suppression on a Flight Research Wing," AIAA Guidance and Control Conference, 1977.
8. Abel I, Newsom, J. R., Dunn, H. J., "Application of Two Synthesis Methods for Active Flutter Suppression on an Aeroelastic Wind Tunnel Model," AIAA paper No. 79-1633, AIAA Atmospheric Flight Mechanics Conference, August 1979.
9. Abel, I. : An Analytical Technique for Predicting the Characteristics of a Flexible Wing Equipped with an Active Flutter-Suppression System and Comparison with Wind-Tunnel Data. NASA TR-1367, February 1979.
10. Anonymous, : Military Specification Flying Qualities of Piloted Airplanes," MIL-F-8785B (ASG), August 1969.
11. Sirisina, H. R., "Optimal Control of Saturating Linear Plants for Quadratic Performance Indices," Int. J. Control, Vol. 8 (1968), pp 65-87.
12. Kwakernaak, H. and Sivan, R., "Linear Optimal Control Systems," John Wiley and Sons, 1972.
13. Johnson, Timothy L., "The Aerodynamic Surface Location Problem in Optimal Control of Flexible Aircraft," MIT Report ESL-R-387, 6-69.
14. Harvey, C. A. and Pope, R. E., "Study of Synthesis Techniques for Insensitive Aircraft Control Systems," NASA CR-2803, April 1977.

15. Brown, R. G., "Linear State Space Analysis," Ph.D Thesis, Iowa State University, June 1967.
16. Doyle, J. C., "Guaranteed Margins for LQG Regulators," IEEE Trans Auto. Control, August 1978.
17. Doyle, J. C., and Stein, G., "Robustness with Observers," IEEE Trans. Auto. Control, TBD 1979.
18. Safonov, M. G., and Athans, "Gain and Phase Margin of Multiloop LQG Regulators," "IEEE Trans. Auto Control," April 1977.
19. Doyle, J. C., "Robustness of Multiloop Linear Feedback Systems," IEEE Conference on Decision and Control, 1978.
20. Petar V. Kokotovic and Richard A. Yackel, "Singular Perturbation of Linear Regulators: Basic Theorems," IEEE Trans. Auto. Ctrl., Volume AC-17, No. 1, February 1972, pp. 29-37.
21. Richard A. Yackel and Petar V. Kokotovic, "A Boundary Layer Method for the Matrix Riccati Equation," IEEE Trans. Auto. Ctrl., Volume AC-18, No. 1, February 1973, pp. 17-24.

DO NOT REMOVE SLIP FROM MATERIAL

Delete your name from this slip when returning material to the library.

NAME	DATE	MS
H. MOSZAK	4/19/94	489
		185